Novel biomass-derived materials as efficient electrocatalysts for O$_2$ reactions

Inês Sequeira Ribeirinha Marques

Mestrado em Química

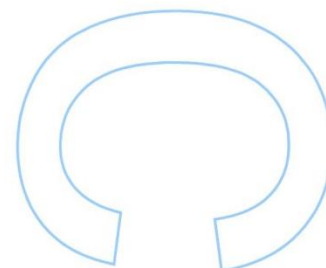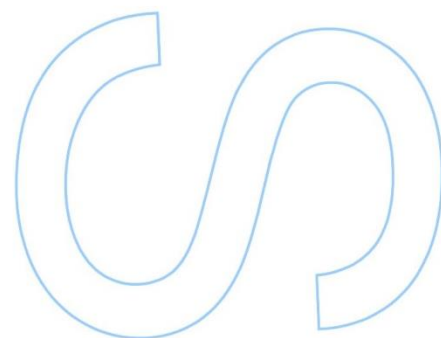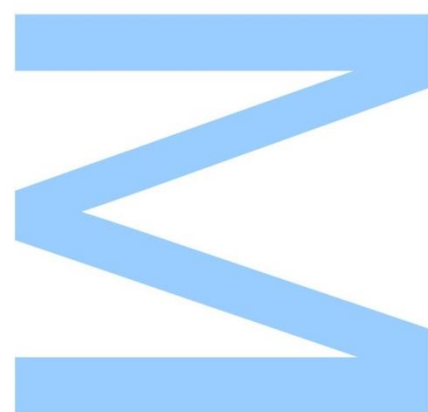Departamento de Química e Bioquímica

2021

Orientador

Professor Doutor Luís Miguel de Brito e Cunha Álvares Ribeiro, Professor auxiliar, Faculdade de Ciências da Universidade do Porto

Coorientador

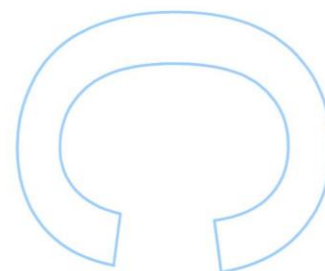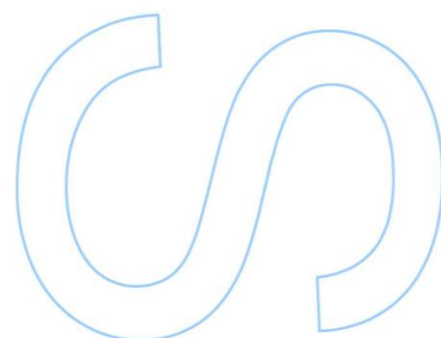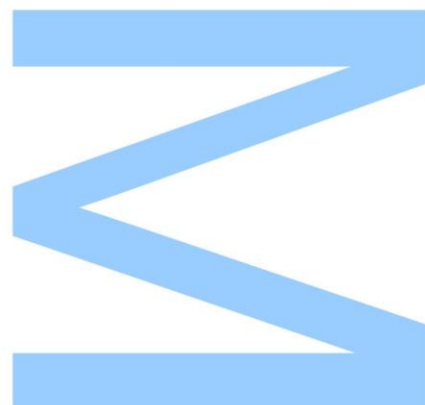Doutora Diana Mónica de Mesquita Sousa Fernandes, Investigadora Auxiliar, LAQV-REQUIMTE

U.PORTO

FC FACULDADE DE CIÊNCIAS
UNIVERSIDADE DO PORTO

Todas as correções determinadas

pelo júri, e só essas, foram efetuadas.

O Presidente do Júri,

Porto, _____/_____/_____

Acknowledgments

This wasn´t possible without the help and support of many people. I would like to express my deepest gratitude in specially,

To Professor Luís Ribeiro, for the opportunity to develop this project and for all the valuable knowledge passed.

To Doctor Diana Fernandes, this was not possible without you. Thank you for all support, dedication, and critical suggestions. You help me grow as a scientist. I will be forever grateful for everything you taught me.

To Doctor Andreia Peixoto and Doctor Rubén Velarde for the scientific and technical orientation and for the assistance provided.

To Aleksey Yaremchenko, CICECO- Aveiro Institute of Materials Department of Materials and Ceramic Engineering (DEMaC), University of Aveiro, for the willingness to do the XRD.

To REQUIMTE-LAQV and Department of Chemistry and Biochemistry of the Faculty of Sciences, University of Porto, for providing me the conditions to develop this project.

To Filipa Santos, it was a pleasure to share this adventure with you.

To my friends, for all the good moments that made these years even better.

To my family, in specially to my father, mother and brother, to all the patient and support.

To Xico, for always being by my side in the writing of this thesis.

To my boyfriend, Hugo Fonseca, one more complete step beside you. Thank you for always supporting me, all the love and patience. Has been a beautiful journey and will continue with more achievements together.

Abstract

The incessant and drastic growth of global energy demand makes it imperative to develop new affordable high-quality materials at a large scale to act as powerful electrocatalysts (ECs) on clean energy storage and conversion devices. Among these, fuel cells (FCs) and electrolyser have emerged as strong candidates. However, their application has been hampered due to the use of noble metal-based electrocatalysts. In this context, this project aims to design and prepare a new generation of sustainable, stable, and high-performance materials, prepared from natural and renewable sources (biochar obtained from vineyard pruning waste) to act as electrocatalysts for the demanding electrochemical reactions of oxygen – oxygen reduction reaction (ORR) and oxygen evolution reaction (OER). Biochar is a low-cost carbon-rich material with promising future applications. It can be easily prepared from the thermochemical degradation of biomass. Due to the unique chemical structure, it can be activated or functionalized, and explored for oxygen reduction reaction and oxygen evolution reaction.

All materials prepared demonstrated moderate ORR electrocatalytic performance in alkaline medium with diffusion-limiting current densities between -3.48 (Co/N-BioC) and -1.27 mA cm^{-2} (Cu/N-BioC) and potential onset values of 0.88 ≥ E_{onset} ≥ 0.66 V vs. RHE. Additionally, the materials tested showed selectivity towards indirect pathway where O_2 is reduced to H_2O_2 and then further reduced to water with the number of electrons transferred per O_2 molecule ranging between 2.1 and 3.6 electrons. The materials also presented moderate OER electrocatalytic performances in alkaline medium, with overpotential values between 0.48 (Co/N-BioC) and 0.63 V vs. RHE (Fe/N-BioC) and maximum current densities between 0.28 (BioC) and 42.60 mA cm^{-2} (Co/N-BioC).

Keywords: Fuel cells, electrochemistry, oxygen reduction and evolution reactions, biomass, biochar.

Resumo

O crescimento incessante e drástico da procura global de energia torna imperativo o desenvolvimento de novos materiais de alta qualidade a preços acessíveis em grande escala para atuar como poderosos eletrocatalisadores (EC) em dispositivos de armazenamento e conversão de energia limpa. Entre estes, as pilhas de combustível (FCs) e a eletrólise da água surgiram como fortes candidatos. Contudo, a sua aplicação tem sido dificultada devido à utilização de eletrocatalisadores à base de metais nobre. Neste contexto, este projeto visa conceber e preparar uma nova geração de materiais sustentáveis, estáveis e de alto desempenho, preparados a partir de fontes naturais e renováveis (biochar obtido a partir de resíduos da poda das videiras) para atuarem como eletrocatalisadores para as exigentes reações eletroquímicas de oxigénio - reação de redução do oxigénio (ORR) e reação de evolução do oxigénio (OER). O biochar é um material rico em carbono, de baixo custo e com aplicações futuras promissoras. Pode ser facilmente preparado a partir da degradação termoquímica da biomassa. Devido à sua estrutura química única, pode ser ativado ou funcionalizado, e explorado para a reação de redução do oxigénio e reação de evolução do oxigénio.

Todos os materiais preparados demonstraram um desempenho eletrocatalítico moderado para ORR em meio alcalino, com densidade de corrente limitada pela difusão entre -3,48 (Co/N-BioC) e -1,27 mA cm^{-2} (Cu/N-BioC) e o potencial onset de 0,88 ≥ E_{onset} ≥ 0,66 V vs. RHE. Além disso, os materiais testados mostraram seletividade para a via indireta onde o O$_2$ é reduzido a H$_2$O$_2$ e depois reduzido a água, com o número de eletrões transferidos por molécula de O$_2$ variando entre 2,1 e 3,6 eletrões. Os materiais também apresentaram desempenhos eletrocatalíticos moderados de OER em meio alcalino, com valores de sobrepotencial entre 0,48 (Co/N-BioC) e 0,63 V vs. RHE (Fe/N-BioC) e densidades máximas de corrente entre 0,28 (BioC) e 42,60 mA cm^{-2} (Co/N-BioC).

Palavras-chave: Pilhas de combustível, eletroquímica, reações de redução e evolução do oxigénio, biomassa e biochar.

Table of Contents

List of Figures

List of Tables

List of abbreviations and symbols

CA	Chronoamperometry
C_{O2}	Bulk concentration of O_2
CHNS	Carbon hydrogen and nitrogen analyser
CV	Cyclic voltammetry
D_{O2}	Diffusion coefficient of O_2
E	Electric potential
E°	Standard electric potential
$E^{\circ}_{Ag/AgCl}$	Standard electric potential vs. Ag/AgCl
$E_{Ag/AgCl}$	Electric potential vs. Ag/AgCl
ECs	Electrocatalysts
E_{onset}	Onset potential
E_{pc}	Potential of the cathodic peak
E_{pa}	Potential of the anodic peak
E_{RHE}	Electric potential vs. RHE
E_{10}	Required potential to reach $j = 10$ mA cm^{-2}
F	Faraday's constant
FCs	Fuel cells
HER	Hydrogen evolution reaction
HOR	Hydrogen oxidation reaction
ICP-OES	Inductively coupled plasma optical emission spectroscopy
j	Current density
$j_{1.8}$	Current density at $E = 1.8$ V vs. RHE
j_k	Kinetic current density
j_L	Diffusion-limited current density
j_{max}	Maximum current density
K-L	Koutecky-Levich
LSV	Linear sweep voltammetry
n_{O_2}	Number of electrons transferred per O_2 molecule
OER	Oxygen evolution reaction
ORR	Oxygen reduction reaction
RDE	Rotating disk electrode
RHE	Reversible hydrogen electrode
RRDE	Rotating ring disk electrode
SEM	Scanning electron microscopy

TS	Tafel slope
XRD	X-ray diffraction
wt%	Concentration expressed as weight percent
v	Scan rate
η	Overpotential
η_{10}	Overpotential to achieve $j = 10$ mA cm^{-2}
ω	Angular velocity

Chapter 1-Introduction

1. Introduction

1.1. Scope and goals of this work

Electrochemical energy conversion is an area in which novel functional materials are the key to the success. In this frame, this project aims at designing and preparing a new generation of sustainable, high-performance, and low-cost materials composed of biochar, obtained from vinery pruning wastes, that after heteroatom doping and/or functionalization with earth abundant metals/metal oxides can serve as efficient electrocatalysts for the oxygen reduction reaction (ORR) and oxygen evolution reaction (OER).

The work plan started with the preparation of the novel biomass-derived materials from vinery pruning wastes by hydrothermal carbonization. The novel composite materials are based on heteroatom-doped biochar material (*in situ* heteroatom doping with N and N/S) and metal-supported biochar (functionalized by the incorporation of Co, Cu, Fe, Ni, Pd, V and Zn in N-doped biochar). Then, the prepared materials were characterized by different techniques such as, carbon hydrogen and nitrogen analyser (CHNS), inductively coupled plasma optical emission spectroscopy (ICP-OES), scanning electron microscopy (SEM) and X-ray diffraction (XRD). Finally, electrocatalytic studies were then performed to evaluate the applicability of the prepared materials as electrocatalysts for ORR and OER.
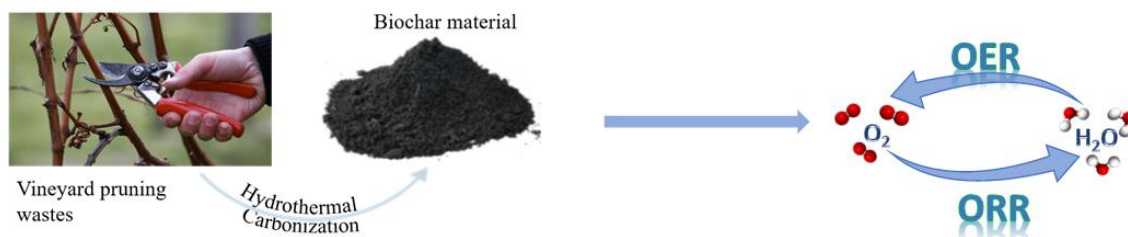
Figure 1 – Schematic illustration of production and application of biochar.

1.2.   The world energy problem

The global energy demand and the continuous consumption of fossil fuel sources has had a tremendous impact on our planet´s ecosystems and biodiversity and has posed serious challenges to energy security, pollution, and climate change. So, it is of upmost importance to develop cost-effective and environmentally sustainable solutions to meet and address these challenges. In this regard, energy storage and conversion technologies will be a promising alternative to reduce this crisis. Some of these technologies includes fuel cells (FCs) and water splitting ($2H_2O \leftrightarrow 2H_2 + O_2$) devices where electrochemistry plays a vital role as their core relies on electrochemical reactions: oxygen reduction (ORR), oxygen evolution (OER), hydrogen oxidation (HOR) and hydrogen evolution (HER).[1-3]   As their efficiencies are significantly dependent on the electrocatalysts (ECs) used, the development of novel low-cost, high performance, industrially and economically attractive, and scalable materials is mandatory.[4, 5]

The Earth's atmosphere provides H_2O, CO_2 and N_2, that can be converted into the products via electrochemical processes coupled to renewable energy if electrocatalysts with the required properties can be developed.[6] In Figure 2, it is possible to observe that important fuels and chemicals (H_2, NH_3 and $C_xH_yO_z$) can be produced by replacing or working in concert with conventional energy production.[7]
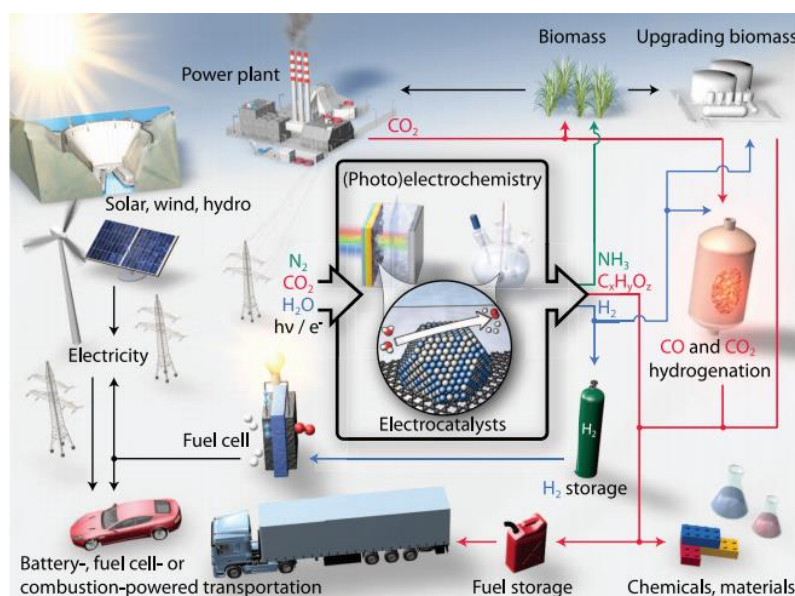
Figure 2 - Schematic of electrochemical processes and their applications. Reproduced from ref. [7]

Fuel cells (FCs) are electrochemical devices that convert the chemical energy of different fuels directly into electrical energy at high efficiency and without combustion processes.[8] Via electrochemical reactions, the fuel and oxygen react and produce electrical energy, CO_2, H_2O, and some waste heat.[9] FCs have high energy conversion efficiency (~80%), and are also small, silent, and have much lower environmental impacts compared to other conventional devices or technologies specifically during the operational phase.[10] With these characteristics, FCs have a wide use in the areas of transport, generation of stationary and portable energy, and will also help to solve the global problems of energy supply and contribute to a cleaner environment.[11-13] In fuel cells, at the anode, the fuel (methanol or hydrogen) suffers electrocatalytic oxidation and at the cathode occurs the reduction of oxygen. The performance of FCs decreases, because it is necessary to apply high reduction potentials due to the involved slow multi-electron reactions.[13, 14]
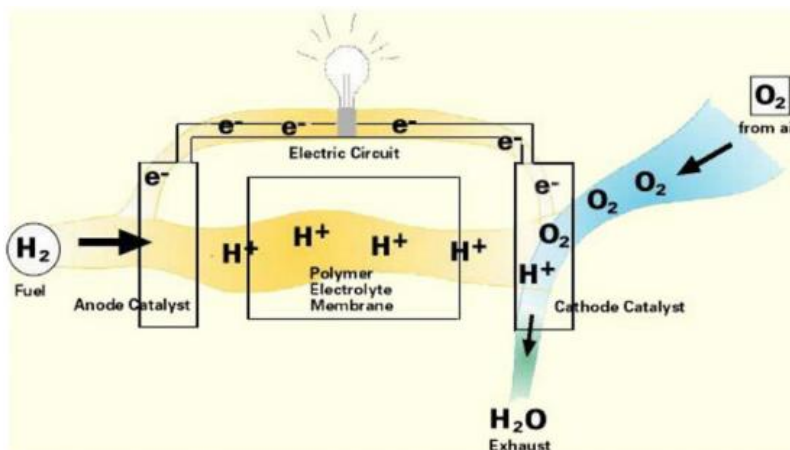
Figure 3 – Schematic representation of the working principle of a fuel cell. Reproduced from ref. [15]

1.3.   Oxygen reduction and evolution reactions

As referred above, the four important electrochemical processes for clean energy conversion are: ORR and HOR that occur at the cathode and anode of fuel cells, respectively, and the HER and OER at the cathode and the anode of an electrolytic cell, respectively. [16-18] The fuel cell (Figure 4 (b)) is an environmentally friendly electrochemical cell that generates energy from O_2 and H_2, leaving water as clean by-product,[19] and the electrocatalytic cell (Figure 4 (a)) uses electricity to split the water into H_2 (fuel) and O_2: $2H_2O$ (l)→$2H_2$ (g)+O_2 (g).[6]
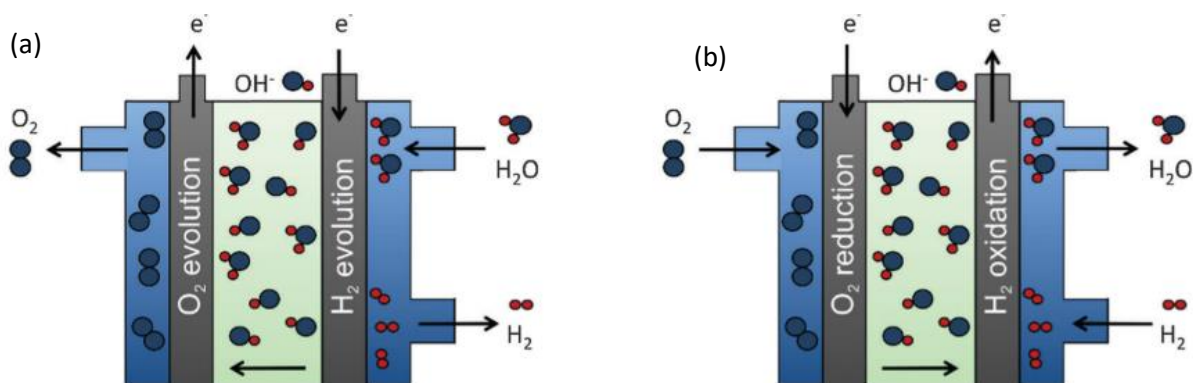
Figure 4 – Schematic illustration of a (a) electrolyser and (b) fuel cell in basic medium. Adapted from ref. [20]

Figure 5 shows the overpotentials and overall reaction equations associated with oxygen-based and hydrogen-based electrochemical reactions. It is possible to notice that oxygen reactions require high overpotentials, which is why oxygen electrocatalysis limits the energy efficiency and the rate capability of electrochemical energy devices. [20, 21]
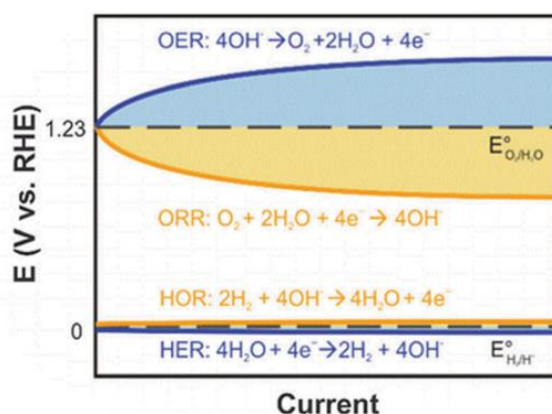
Figure 5 – Schematic of the overpotentials associated with hydrogen electrocatalysis (HER, HOR) and oxygen electrocatalysis (ORR, OER) and their overall reaction equations. Reproduced from ref. [20, 21]

To evaluate the ORR and OER performance, the two most important techniques are cyclic voltammetry (CV) and linear sweep voltammetry (LSV). CV (Figure 6 (a)) can quickly provide qualitative information about the electrocatalysts and electrochemical reactions, such as the electrocatalyst electrochemical response, its interaction with the electrode, and the electrocatalyst catalytic activity. For ORR, a linear potential sweep is applied to a working electrode at a steady scan rate, first from a positive potential to a negative potential and subsequently in the reverse direction. [22, 23] In LSV (Figure 6 (b)), the working electrode potential is changed linearly with time, starting from a potential where no electrode reaction occurs and moving to potential values at which the analyte reduction (more negative values) or oxidation (more positive values) takes place. [24]
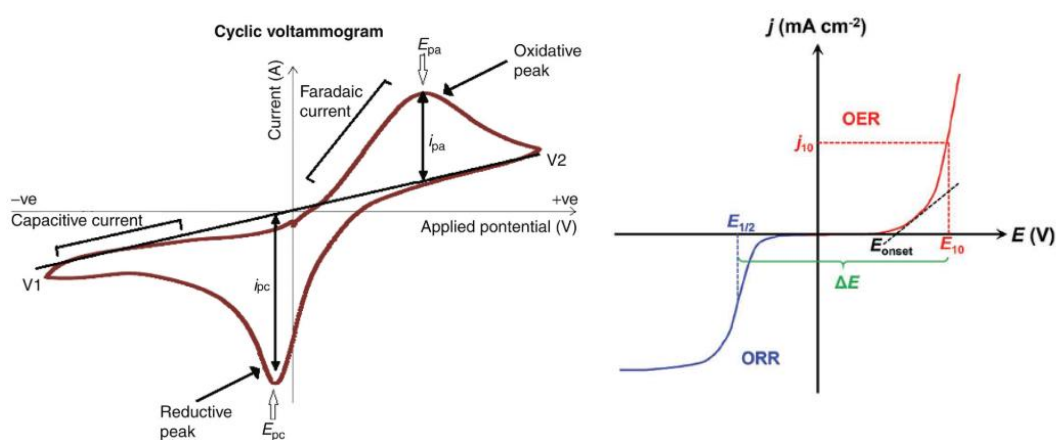
Figure 6 – (a) A schematic diagram of a cyclic voltammogram. Reproduced from ref.[23] (b) Polarization curves for ORR and OER. Reproduced from ref. [25]

1.3.1. Oxygen Reduction Reaction

The electrocatalytic ORR is the most challenging reaction in fuel cell and metal-air battery technologies. In aqueous and basic electrolytes, O_2 molecule can be reduced through:[6]

(i) A direct four-electron (4e⁻) pathway, where a molecule of O_2 gains directly 4e⁻, producing hydroxide ions without the involvement of H_2O_2.

$$O_2 + 4e^- + 2H_2O \rightarrow 4OH^-$$
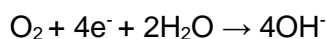
(ii) An indirect pathway involving two steps of two electrons (2e⁻), where O_2 is reduced to HO_2^- and then further reduced to water.

$$O_2 + H_2O + 2e^- \rightarrow HO_2^- + OH^-$$
$$HO_2^- + H_2O + 2e^- \rightarrow 3OH^-$$
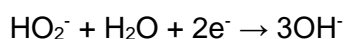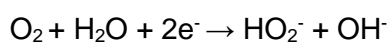
The first direct process is the desired one due to its positive potential which confers a large open circuit potential in FCs and metal-air batteries.[6] For some fewer active materials, two-electron reduction pathway, in which H_2O_2 appears as the final product is also possible and attractive to produce hydrogen peroxide. ORR is a sluggish reaction due to the strong O=O bond that needs to be broken. [26]

The electrochemical parameters that are used to evaluate the performance of ORR electrocatalysts are:

→ **Onset potential (E_{onset})** is the potential at which the reaction starts. It can be calculated by two different ways: 1) the potential at 5% of the maximum current (j_{max}) or 2) the potential at a current density (j) of - 0.1 mA cm^{-2}.

→ **Diffusion-limited current density (j_L)** is the current density reached when the reaction at the electrode is totally controlled by mass transport (a plateau is reached and $j = j_L$).

→ **Kinetic current density (j_k)** is the current in the absence of mass-transfer limitations.

→ **Number of electrons transferred per O_2 molecule (n_{O2})** is determined through the Koutecky-Levich (K-L) equation, from the j^{-1} vs. $\omega^{-1/2}$ plot's slope and provides information about the selectivity of the electrocatalyst (2-electron or 4-electron pathway).

→ **Tafel slope** is usually employed to understand the reaction kinetics and mechanism, which is needed to compare the catalytic activities of different electrocatalysts. [22]

An electrocatalyst with a good performance towards ORR is expected to have a less negative E_{onset}, high j_L value, low Tafel slope and selectivity for the 2- or 4- electron pathway depending on the desired application. It is also desirable that the electrocatalysts exhibit high stability/durability, resistance to CO poisoning and tolerance to methanol crossover (in the case of methanol fuel cells). [6]

1.3.2.   Oxygen Evolution Reaction

OER involves O_2 generation through electrochemical oxidation of water. In alkaline electrolytes the hydroxide ions are oxidized giving rise to H_2O and O_2. [6]

$$4OH^- \rightarrow 2H_2O\,(l) + O_2\,(g) + 4e^-$$
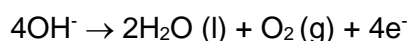
The generally accepted mechanisms for OER comprise a complex multistep proton coupled electron transfer and oxygen-oxygen bond formation and involve several surface adsorbed intermediates. Therefore, the overall reaction rate depends on the kinetic constraints of the elementary reaction steps, which depend on the relative stability of each intermediate

and of the activation barriers between them and generally results in a sluggish kinetics and large overpotential. [6]

To fairly evaluate the performance of OER electrocatalysts, there are some kinetic parameters that are commonly utilized, such as:

→ **Overpotential (η_{10})** is the difference between the potential at which a j = 10 mA cm^{-2} is obtained and the standard value of 1.23 V vs. RHE. The j = 10 mA cm^{-2} value usually used is the current density expected for a 12.3 % efficiency in solar to hydrogen devices, a requirement for cost-competitive photoelectrochemical water splitting.

→ **Maximum current density (j_{max})** is the potential at the last E used.

→ **Tafel slope,** as for the ORR is usually employed to understand the reaction kinetics and mechanism, which is needed to compare the catalytic activities of different electrocatalysts.[22, 27, 28]

A low Tafel slope and a low overpotential are expected for a good OER electrocatalyst.[6, 22]

A four-electron process is involved in OER, resulting in the sluggish nature and slow reaction kinetics of OER. Therefore, high-performance electrocatalysts are required to accelerate the OER and reduce the overpotential. [29]

1.4. Novel biomass-derived materials

Platinum-based materials are recognized as the most active electrocatalysts for ORR because just a small amount of Pt is required to accelerate the conversion process [30] however, the same doesn't apply for OER having poor electrocatalytic activity because Pt oxidizes easily at large overpotentials. For OER the most effective electrocatalysts are RuO$_2$, and IrO$_2$, that on the other hand have poor ORR activity. Moreover, due to their high cost, low abundance, low selectivity, poor stability and durability, easy corrosion, and intolerance to fuel crossover (methanol and CO), many efforts have been made to develop efficient and cost-effective electrocatalysts.[31-34]

Carbon materials, more specifically fullerenes, graphene and carbon nanotubes are also widely used in electrochemical energy storage and conversion devices.[35, 36] These materials, as electrocatalysts, have numerous advantages such as, high specific surface area, symmetrical pore size and structure, high electric conductivity, and strong mechanical properties. However, these are difficult to synthesize and awfully expensive for massive production. Additionally, another disadvantage is the fact that conventional carbon materials are produced from petrochemical products via energy-intensive or harsh synthetic processes. [37, 38]

One way to improve carbon materials performances is through doping with different heteroatoms like nitrogen, boron, sulphur or phosphorous. Doping can tune the electronic

properties of pristine carbon materials giving rise to increased performances. [39, 40] From all the heteroatoms that can be used for doping, nitrogen is, by far, the most popular due to its similar size and the presence of an additional electron in the external shell. It also has other advantages such as simple doping processes with effective modulation of the graphitic structure and properties, simultaneously yielding high electrical conductivity.[41] Additionally, doping modifies the atomic scale structures, and the charge distribution of the carbon atoms is disturbed which generates active sites on carbon materials that can act as anchoring sites to attach other species. [42, 43] For example, electrocatalysts with C-M-N_x (M=Co, Fe, Ni) have been developed and are promising for ORR and OER by incorporation of iron [44], cobalt [45], or nickel [46] with nitrogen-rich polymer precursors, such as phenanthroline, under high temperature processes. The use of inexpensive transition metals to replace precious metals can reduce costs and facilitate large-scale application. [47-49]

Recent developments show that research on N-doped carbon materials has shifted from expensive and dangerous inorganic and organic chemicals to renewable biomass, taking sustainability into account.[50] Biomass is a clean, abundant, renewable, low-cost, widespread, and eco-friendly resource.[51-53] So, as an alternative to conventional carbon materials, biomass-derived materials have been explored as electrocatalysts for ORR and OER in energy storage and conversion devices, due to their different sources, for example, agriculture crops and residues. [54, 55]

Biochar is defined as a carbon-rich, porous solid produced by heating biomass (thermochemical degradation processes, like pyrolysis, gasification, and hydrothermal carbonization), manure with little or no oxygen at moderate temperatures (350-800 °C). Therefore, is cheaper to produce than conventional carbon materials.[10, 38, 51, 56-58]

Due to its surface morphology, such as pore distribution and structure, large specific surface area, abundant surface functional groups (C-O, C=O, COOH, and OH), mineral components (N, S, P, Ca, Mg and K), high electrical conductivity, porosity stability and good hydrophilicity, biochar can be used as an electrode material in fuel cells.[10, 56, 57, 59]

One way to enhance the electrochemical properties of biochar is to do the *in-situ* activation with metals (Fe, Ni, Co, etc) or to dope it with heteroatoms (N, S, B or P), similarly to what has been done with carbon materials like graphene or graphite which has proven to enhance their electrochemical properties.[29, 60] Biochar-based materials can afford advanced matrices with a high surface area and embedded active catalytic sites which can lead to high-performance ORR catalysts. For example, the introduction of iron into nitrogen-doped biomass may facilitate the formation of planar pyridinic- and pyrrolic-N, both of which could provide active sites with enhanced ORR performance through a 4⁻ electron transfer process.[29] The nitrogen-doped biochar can also act as a catalyst support with improved ORR catalytic activity and durability because of the π bonding and the strong electron donor behaviour of N atoms,

confering a larger electronegativity to nitrogen compared to carbon atoms. Nitrogen atoms can create positive charge density on the adjacent C atoms, which results in the highly favourable adsorption of O_2. [61] Additionally, nitrogen-doped carbon materials exhibit an excellent methanol tolerance in alkaline media.[61-63] In Table 1, some examples are given of N-doped biochar-based electrocatalysts derived from catkin, coconut shells, pomelo peel, ginkgo leaves, corn crumb, water hyacinth and microalgae. All the presented electrocatalysts have moderate electrocatalytic activity in terms of onset potential, current density and number of electrons transferred per O_2 molecule and excellent tolerance to methanol crossover and stability.[64]

Table 1– Examples of biochar electrocatalysts for oxygen reduction reaction.

Original Biomass	Biochar	Brief biochar synthesis methods	ORR activity [a]	Ref.
Catkin	Iron and nitrogen co-doped carbon nanotubes@hollow carbon fibers	Add melamine and $FeCl_3$ to catkin and pyrolysis at 800 ºC for 2 h under N_2 flow. Wash with H_2SO_4.	E_{onset}=0.98 V vs. RHE $j_{-0.4 V}$= 4.083 mA cm^{-2} $ñ \approx 3.915$ electrons TS=65.8 mV dec^{-1} Stability= 88.9%	[65]
Coconut shells	Porous N,P-doped carbon from coconut shells	Carbonization at 500 ºC for 1h under N_2 flow. Functionalization with urea, and pyrolysis at 1000 ºC for 2 h.	E_{onset} = -0.02 V vs. Ag/AgCl (E_{onset} = 0.94 V vs. RHE) $ñ \approx 3.7$ electrons Stability= 75%	[66]
Pomelo peel	Nitrogen-doped nanoporous carbon derived from waste pomelo peel (N-PC-1000)	Hydrothermal treatment at 180 ºC for 16h and thermal annealing for 2h at 1000 ºC under NH_3 atmosphere.	E_{onset} = 0.01 V vs. Hg/HgO (E_{onset} =0.94 V vs. RHE) j = - 4.60 mA cm^{-2} Good tolerance to methanol and stability	[67]
Ginkgo leaves	Nitrogen-doped fullerene-like carbon shell (NDCS), where N is derived from Ginkgo leaves	Fallen ginkgo leaves were heated at 80 ºC in an oven for 12 h. The product was annealed at 800 ºC for 2 h at N_2 atmosphere. The final product was washed by 2 mol dm^{-3} HCl.	E_{onset} = 0.156 V vs. Hg/HgO (E_{onset}= 1.087 V vs. RHE) j_L= 3.740 mA cm^{-2} Stability= 89%	[68]
Corn crumb	Biomass-derived WC/N-doped carbon nanocomposite	Added WS_2 and heated to 270 ºC for 24 h. Pre-electrolysis at a cell voltage of 2.4 V for 2h to remove residual impurities. Then, pyrolysis-electrolysis for 24 h at 3.0 V.	E_{onset}=0.87 V vs. RHE $ñ \approx 3.80$ electrons TS=61.52 mV/dec Methanol=70% Stability= 86%	[69]
Water hyacinth	Biomass-derived nitrogen self-doped porous carbon	Pyrolysis at 700 ºC for 2 h with $ZnCl_2$ as an activation reagent under N_2 flow.	E_{onset}=0.98 V vs. RHE j_L= 4.15 mA cm^{-2} $ñ \approx 3.51—3.82$ electrons TS=103.4 mV/dec Stability= 91.2%	[70]
Microalgae	N-doped biochar via an ionic liquid ([Bmin][FeCl4])-assisted microalgae biomass	Ionothermal treatments at 220 ºC, then carbonization at 800 ºC under N_2 flow for several hours (3 to 7 h).	E_{onset}=1.10 V vs. RHE j_L= -5.329 mA cm^{-2} $ñ$ =3.55–3.99 electrons TS=95 mV/dec Methanol =99.9% Stability=91.2%	[71]

[a] TS = Tafel slope

Chapter 2- Experimental section

2. Experimental Section

2.1. Reagents and solvents

Absolute ethanol (99.8%, Fisher Chemical), 1,10-phenanthroline (99+%, Aldrich), vanadyl-acetylacetonate (95%, Aldrich), iron (III) acetylacetonate (97%, Aldrich), palladium (II) acetate (Fluka), zinc acetate-dihydrate (Merck), cobalt (II) acetate tetrahydrate (Merck), nickel (II) acetate tetrahydrate (Riedel-de Haën®), copper (II) acetylacetonate (Acros organics) and elemental sulphur (>99%, Merck) used in the material preparation were used as received.

For the electrochemical studies, the following reagents and solvents were used: potassium hydroxide (KOH, 99.99%, Sigma-Aldrich), platinum nominally 20% on carbon black (Pt/C 20 wt%, HisPEC® 3000, Alfa Aesar), Nafion 117 (5 wt% in lower aliphatic alcohols and water, Aldrich), isopropanol (99.5%, Aldrich), methanol (anhydrous, VWR), ruthenium (IV) oxide (99.9% trace metals basis, Aldrich) and iridium (IV) oxide (99.9% trace metals basis, Aldrich). Ultrapure Water (18.2 MΩ cm at 25°C, Millipore) was used throughout the experiments.

2.2. Materials preparation

2.2.1. Biochar *tinta roriz*

The biomass material used in this research was the vineyard pruning wastes from Vitis vinifera *Tinta Roriz* variety, sampled in *Quinta dos Carvalhais (Mangualde, Dão region)* and kindly supplied by *Sogrape Vinhos, S. A. (Portugal)*. Before any treatment, vineyard pruning wastes were oven-dried at 50 °C for 24 h, ground and sieved to obtain a particle size between 100 and 200 μm.

Solid hydrochar material was produced by hydrothermal carbonization of the vineyard pruning wastes using a high-pressure batch reactor (Parr Instrument Co.) equipped with temperature digital controllers, mechanical stirring system, and gas flow meters. For each run, 40 g of sieved vineyard pruning wastes and 400 mL of deionized water were placed into the 500 mL vessel. The mixer was sealed, stirred continuously at 250 rpm, and heated up to 250 °C using an electric furnace. When this temperature was reached, the inner pressure was stabilized at 45-50 bar (autogenous pressure). After 50 min reaction time, heating and stirring were stopped, the vessel was cooled to room temperature and the as-produced solid hydrochar fraction was recovered by filtration and drying overnight at 100 °C. The as-produced hydrochar was activated by CO_2 carbonization at 800 °C for 30 min and the resulting biochar was labelled as BioC. [72]

The heteroatom-doped biochar material (*in situ* heteroatom doping with N and N/S) and the metal-supported biochar (functionalized by the incorporation of Co, Cu, Fe, Ni, Pd, V, Zn at N-doped biochar) were then prepared as described in the literature. [73]

2.2.2. Heteroatom-doped biochar

Biochar N-doped material was prepared by dissolving 0.291 g of 1,10-phenantroline in 20 mL of ethanol and stirring the mixture at 700 rpm for 90 min at 60 ºC. Then, the biochar *tinta roriz* (0.615 g) was added and the mixture stirred (700 rpm) at room temperature for 22 h. The solvent was then removed under reduced pressure (100 bar) using a rotary evaporator (Büchi Rotavapor R-200) at a temperature of 40 ºC for 2 h. The dried material was grounded to a fine powder and transferred to a suitable crucible with a lid. Finally, the crucible was inserted in the oven chamber (Nabertherm) and pyrolyzed at 800 ºC for 2 h under an N_2 atmosphere. This sample was labelled as N-BioC.

Biochar N/S-doped was prepared using the biochar N-doped (0.300 g) to which 0.06 g of sulphur was added. The material was grounded and transferred to a suitable crucible with a lid and pyrolyze at 800 ºC for 2 h under an N_2 atmosphere. This sample was labelled as N/S-BioC.

2.2.3. Metal-supported biochar

For the preparation of metal-supported biochar, 0.54 mmol of the corresponding acetate precursor (0.134 g of cobalt (II) acetate tetrahydrate, 0.191 g of iron (III) acetylacetonate, 0.152 g of vanadyl acetylacetonate, 0.130 of nickel (II) acetate tetrahydrate, 0.123 g of palladium (II) acetate, 0.141 g of copper (II) acetylacetonate and 0.118 g of zinc acetate-dihydrate) were dissolved in 20 mL of EtOH, by stirring the mixture for 10 min at room temperature and at 700 rpm. Then, 1,10-phenanthroline (0.291 g) was added and the mixture stirred at 60 ºC for 90 min and 700 rpm. The biochar *tinta roriz* (0.615 g) was added and stirred (700 rpm) at room temperature for 22 h. After, the solvent was removed under reduced pressure (100 bar) using a rotary evaporator at a temperature of 40 ºC for 2 h. Before pyrolysis, the dried material was grounded to a fine powder and transferred to a suitable crucible with a lid which was placed into the chamber of the oven and pyrolyzed at 800 ºC for 2 h under an N_2 atmosphere. These samples were labelled as Ni/N-BioC, Pd/N-BioC, Fe/N-BioC, V/N-BioC, Co/N-BioC, Cu/N-BioC and Zn/N-BioC.

For the preparation of biochar with 2 metals, 0.27 mmol cobalt (II) acetate and 0.27 mmol nickel (II) acetate tetrahydrate was used. The method and other reagents and solvents used were the same as referred above. This sample was labelled as Co,Ni/N-BioC.

2.3.   Characterization methods

Fundamental principles and the description of the experimental procedure of the characterization methods are discussed here.

2.3.1.   Carbon hydrogen and nitrogen analyser (CHNS)

CHNS analysers provide a rapid determination of carbon, hydrogen, nitrogen, and oxygen in different types of materials. They require high temperature combustion (1000 ºC) in an oxygen-rich environment. During the combustion process, carbon is converted to carbon dioxide, hydrogen to water, nitrogen to nitrogen gas/ nitrogen oxides and sulphur to sulphur dioxide. If other elements are present, they will also be converted to combustion products. Once formed, the combustion products are swept out of the combustion chamber by inert carrier gas such as helium and passed over heated high purity copper. This copper can be situated at the base of the combustion chamber or in a separate furnace (600 ºC). The function of this copper is to remove residual oxygen not consumed in the combustion and to convert any nitrogen oxides to nitrogen gas. [74, 75]

Experimental procedure: CHNS analyses were performed to rapidly determinate the percentages of carbon, hydrogen, nitrogen, and oxygen using a LECO equipment (CHNS-932 model) with sample size between 0.01-2 mg and a precision and reproducibility lower than 0.03 and 0.2 %, respectively.

2.3.2.   Inductively   coupled   plasma-optical   emission spectroscopy (ICP-OES)

Inductively coupled plasma-optical emission spectroscopy is an analytical technique that is used to identify the atomic composition of a particular sample. The technique makes use of the unique photophysical signals of each element to successfully detect the type and relative amount of each element within the complexity of a sample.[76]

Experimental procedure: Metal content of the ECs was determined by ICP-OES after digestion in HCl acid (37 wt%) and dilution with water (1:10 v/v).

2.3.3. Scanning electron microscope (SEM) and energy dispersive X-Ray spectroscopy (EDS)

Scanning electron microscopy uses a high-energy beam of electrons to obtain information about morphology and topography of the surfaces of solids. When an electron beam contacts the surface of a sample, energy is transferred to the sample atoms, which releases secondary electrons. The observed contrast in a SEM image is due to the emission of secondary electrons from different regions of the surface. [11, 77]

Experimental procedure: SEM/EDS was employed to characterize the morphology and chemical composition of the prepared materials. EDS also allowed to determine the distribution of each element in the samples studied. The instrumentation used for SEM analysis was a Hitachi SU-70 instrument, while for EDS a Bruker Quantax 400 detector equipment, at *Departamento de Engenharia de Materiais e Cerâmica, Universidade de Aveiro* and also Scanning electron microscopy/Energy-dispersive X-ray spectroscopy (SEM/EDS) was carried out using a high resolution (Schottky) environmental SEM with X-ray microanalysis and electron backscattered diffraction analysis (Quanta 400 FEG ESEM/EDAX Genesis X4M), in high-vacuum conditions, at the *Centro de Materiais da Universidade do Porto (CEMUP).*

2.3.4. X-Ray Powder Diffraction (XRD)

X-Ray diffraction provides knowledge about arrangement and spacing of atoms in crystalline materials and physical properties of metals, polymeric materials, and other solids. The X-Ray photons interact with the electrons of the atoms in the crystal and are diffracted, or scattered. [11, 77]

Experimental procedure: The XRD was used to study the structure and composition of biochars. The ECs were characterized by X-Ray diffraction on a PANalytical X'Pert Pro diffractometer equipped with Cu Kα radiation (λ = 1.5405 Å). Wide-angle diffractograms were collected over the range 10° < 2θ < 80° with a step size of 0.02° and counting time 200 s.

2.4.   Electrochemical performance

For the electrochemical studies (OER and ORR), an Autolab PGSTAT 302N potentiostat/galvanostat (EcoChimie B.V.), controlled by Nova v2.1 software, was used. All ORR electrochemical studies were performed at room temperature, using a conventional cell with a three-electrode compartment: (a) reference electrode: Ag/AgCl (3 mol dm^{-3} KCl, Metrohm); (b) working electrode: modified glassy carbon rotating disk electrode, RDE, (glassy carbon, electrode disk diameter 3 mm, Metrohm) and (c) auxiliary electrode: carbon rod (2 mm in diameter, Metrohm). For OER, the reference electrode and working electrode were the same as ORR, but the counter electrode was a platinum wire (d = 0.6 mm, l = 0.5 m, 99.99+%, Goodfellow).

For the peroxide production test (ORR), the RDE was replaced by a rotating ring disk electrode, RRDE (5 mm disc of glassy carbon with a concentric platinum ring, Metrohm) consisting of a glassy carbon disk and a platinum ring.

Before modification, the RDE was conditioned by a polishing process using three diamond pastes of grain sizes of 6, 3 and 1 µm (Buehler, MetaDI II), on a Nylon polishing disc (Basi Analytical Instruments). When the RRDE was used, the cleaning procedure was performed only with 0.3 µm alumina powder (MicroPolish Alumina, Buehler) to prevent damage of the Pt ring.

The ECs dispersion used for electrode modification were prepared as follows: 1 mg of the selected material or Pt/C were mixed with 125 µL of isopropanol + 125 µL of ultrapure water + 20 µL of Nafion 117. To achieve a more uniform dispersion, the mixture was placed in an ultrasound bath (Fisherbrand, FB11201) for at least 15 minutes.

For the electrode modification (Figure 7), two drops of 2.50 µL of the selected dispersion were placed onto the surface of the RDE and allowed to dry under a constant flow of hot air.

All electrocatalytic studies were performed using a KOH solution (0.1 mol dm^{-3}, 100 mL) in an atmosphere saturated with N_2 or O_2. To guarantee saturation of the electrolyte solution with the desired gas, it was passed through for at least 30 minutes.

Dispersion:
1 mg of selected material or Pt/C
+ 125 µL isopropanol
+ 125 µL ultrapure water
+20 µL Nafion 117

2 disperson
drops of 2.50 µL
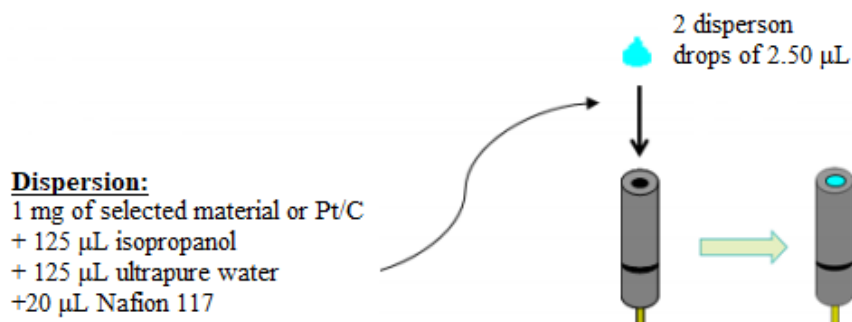
Figure 7 – Electrode modification procedure.

2.4.1. ORR electrochemical performance

Electrocatalytic performance of the biochars toward ORR was studied by cyclic voltammetry and linear sweep voltammetry. The scan rate for both was 5 mV s^{-1}, and the rotation speeds used for LSV were 400, 800, 1200, 1600, 2000 and 3000 rpm.

The effective ORR current was obtained by subtracting the current obtained in N_2-saturated KOH electrolyte by that obtained in O_2-saturated.

The E_{onset} vs. Ag/AgCl were converted to E_{onset} vs. RHE (reversible hydrogen electrode) using the following Equation 1:

$$E \text{ (RHE)} = E_{\text{(Ag / AgCl)}} + 0.059\text{pH} + E^{\circ}_{\text{(Ag / AgCl)}} \quad (1)$$

where $E_{\text{(RHE)}}$ is the potential vs. RHE; $E^{0}_{\text{(Ag / AgCl)}}$ = 0.1976 V (25 ºC), and $E_{\text{(Ag/AgCl)}}$ is the potential measured vs. Ag/AgCl.

The Koutecky-Levich (K-L) Equation (2) was used to analyse the LSV data, and the number of electrons transferred per molecule of O_2 (n_{O2}) in the oxygen reduction reactions was determined by the slopes of the K-L graphs:

$$\frac{1}{j} = \frac{1}{j_L} + \frac{1}{j_k} = \frac{1}{B\omega^{1/2}} + \frac{1}{j_K} \quad (2)$$

with j = current density measured, j_L = diffusion-limited current density, j_K =kinetic current density and ω= angular velocity. The parameter B is associated to the diffusion limiting current density expressed by the Equation 3:

$$B = 0.2n_{O_2}F(D_{O_2})^{\frac{2}{3}}v^{-\frac{1}{6}}C_{O_2} \quad (3)$$

F = 96 485 C mol^{-1}, D_{O_2} = O_2 diffusion coefficient, v = electrolyte kinematic viscosity and C_{O_2} = O_2 bulk concentration. For rotation speeds in rpm is adopted a constant 0.2. Additionally, in the electrolyte used (KOH 0.1 mol dm^{-3}): D_{O_2} = 1.95×10^{-5} cm^2 s^{-1}, v = 0.008977 cm^2 s^{-1} and C_{O_2} = 1.15×10^{-3} mol dm^{-3}.

The Tafel plots ($E_{(RHE)}$ vs. log j_k) were obtained after the LSV currents were corrected for diffusion to obtain the respective kinetic currents. The parameter j_L, determined by the combination of equations 2 and 3, was used to achieve the mass transport correction. The values of j_k obtained were normalized by the mass of the electrocatalyst. [13]

The rotating ring disk electrode measurements in KOH O_2-saturated solution were also performed to obtain a more in-depth information about the electrocatalytic activity of the compounds under study. The H_2O_2 percentages were determined by the ring current (platinum, i_R), the disc current (i_D), and the platinum ring efficiency parameter (N = 0.25 in this case) using equation 4:

$$\% \ H_2O_2 = 200 \ \times \ \frac{i_R/N}{i_D + i_R/N} \qquad (4)$$

Methanol resistance was carried out by chronoamperometry in O_2- saturated KOH for 2500 s, at a fixed potential of E = -0.55 V vs. Ag/AgCl and speed rotation of 1600 rpm, where, at 500 s, 2 mL of methanol was added to the electrolyte. Stability tests were also conducted by chronoamperometry in O_2-saturated KOH for 20 000 s, at a E = - 0.55 V vs. Ag/AgCl and 1600 rpm. [78]

2.4.2.   OER electrochemical performance

Oxygen evolution tests were performed in N_2-saturated alkaline electrolyte, 0.1 mol dm^{-3} KOH solution purged with N_2 for at least 30 min before the measurement. Linear sweep voltammograms were obtained by sweeping the potential from 1.0 to 1.8 V (vs. RHE) at a scan rate of 5 mV s^{-1} and at 1600 rpm of rotation speed. All presented LSV tests were performed with i_R-compensation, via previous calculation of the uncompensated resistance (R_u) of the circuit using the i-interrupt approach, and finally, applying an i_R-compensation value equal to 0.90×R_u to the LSV measurement. To study the OER activity of the heteroatom-doped and metal-supported biochar, Tafel slopes were calculated by linear fitting of LSV data to the following equation:

$$\eta = a + b \times \log|j| \qquad (5)$$

where η stands for the overpotential, b corresponds to the Tafel slope, and j is the current density.[79] Stability tests were evaluated by chronoamperometry in N_2-saturated KOH for 45 000s, at 1.70 V vs. RHE and 1600 rpm. [80]

Chapter 3- Results and discussion

3. Results and discussion

3.1. Characterization

3.1.1. Carbon hydrogen and nitrogen analyser

Prior to further use, the hydrochar was activated by CO_2 carbonization at 800 °C for 30 min and both samples, the hydrochar and the biochar (BioC), were analysed by CHNS (Table 2). This activation step is important to improve the properties of biochar, such as significant adsorption in gas and liquid phases due to its high micropore volume, large specific surface area, favourable pore size distribution, thermal stability, and capability for rapid adsorption. [81] As expected, carbon is the major element with 60.6 % for hydrochar and 80.4% for the activated BioC. This increase of carbon amount from the hydrochar to BioC is due to the carbonization process under CO_2 atmosphere. The percentages of hydrogen and oxygen also decreased, and this can be explained by the loss of structural water that is released during carbonization. Regarding the percentage of nitrogen, no significant differences can be observed with values of 0.8% and 0.9% for hydrochar and BioC, respectively. As only BioC underwent carbonization, it is the only sample that presents moisture and ash, with percentages of 2.0% and 4.6%, respectively.

The changes that occurred are related to the vineyard pruning wastes composition and the activation process used. It is known that the vineyard pruning wastes consist of hemicellulose, cellulose, and lignin and to obtain activated carbon from it, the polymers must be decomposed by a carbonization process. Lignin starts decomposition at low temperatures (160 – 170 ºC) and continues to decompose at low rate until approximately 900 ºC. Hemicellulose is the second component to start decomposing, followed by cellulose, in a temperature interval from about 200 to 400 ºC.[82] As a result of decomposition, volatile compounds such as hydrogen, oxygen and nitrogen leave and biochar become enriched in carbon. [83]

Table 2– Percentages of carbon, hydrogen, nitrogen, and oxygen of hydrochar and BioC.

	Hydrochar	BioC
C	60.6	80.4
H	5.5	1.3
N	0.8	0.9
O	27.5	5.9
Moisture	n/D	2.0
Ash	n/D	4.6

3.1.2. Inductively coupled plasma-optical emission spectroscopy

The metal content of all metal-supported BioC was confirmed by ICP-OES analysis. It was determined from the data in Table 3 and equations 6 and 7. The percentages of metal are represented in Figure 8. ICP-OES analysis also confirmed that biochar with cobalt and nickel has the same proportion of both metals.

$$\text{Final concentration} = \text{Sample concentration Sample} * \frac{\text{Final Volume}}{\text{Sample weight}} \qquad (6)$$

$$\text{wt\%} = \frac{\text{Final concentration}}{10000} \qquad (7)$$

Table 3– ICP-OES data of the different biochars.

Sample	Metal	Sample concentration (mg/L)	Sample Weight (g)	Final Volume (mL)	Final concentration (mg/kg)
Ni/N-BioC	Ni	12.754	0.00241	10	52921
Pd/N-BioC	Pd	8.922	0.00221	10	40373
Fe/N-BioC	Fe	9.053	0.00226	10	40056
V/N-BioC	V	11.067	0.00244	10	45356
Co/N-BioC	Co	14.050	0.00267	10	52622
Cu/N-BioC	Cu	7.991	0.00239	10	33436
Zn/N-BioC	Zn	4.108	0.00258	10	15922
Co,Ni/-BioC	Co	5.793	0.00612	25	23664
	Ni	5.709	0.00612	25	23321
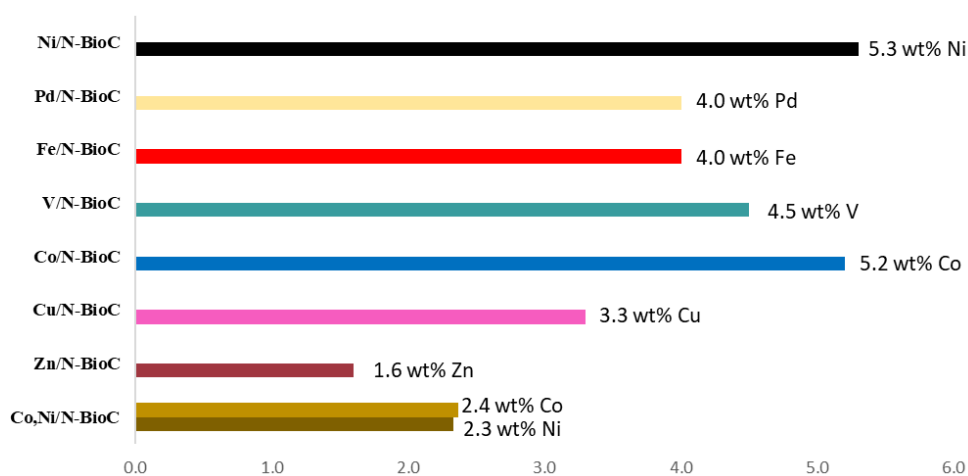
Figure 8 – Metal concentrations for the different electrocatalysts, obtained by ICP-OES.

3.1.3. Scanning electron microscopy (SEM) and energy dispersive X-Ray spectroscopy (EDS)

3.1.3.1. BioC

The morphology of all the materials prepared was assessed by SEM. Since the analyses were performed at two different centres due to several constraints (equipment failure and Covid-19 situation) the discussion is made separately for each material as the analysis conditions were not always the same. Figure 9 (a) and (b) depicts the SEM images for BioC at a magnification of 5 000× at SE mode. Due to the activation step with CO_2, BioC presents high porosity as shown in Figure 9 (a). The elements present in the sample were analysed by EDS (Figure 9 (c)) and several were detected: carbon, oxygen, magnesium, aluminium, silicon, phosphorous, sulphur, potassium, and calcium. These elements are in accordance with those described in the literature for the different types of BioC.[56]
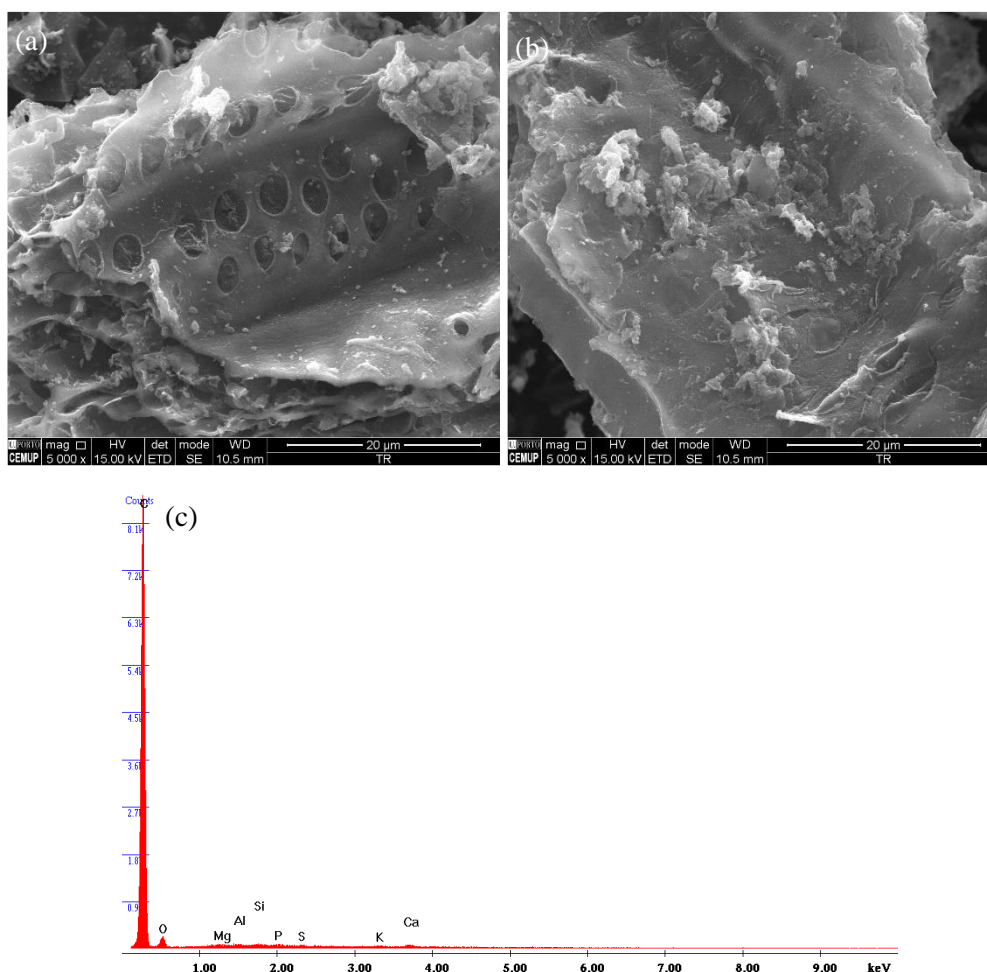
Figure 9 – (a) and (b) SEM images at magnification of 5 000× at mode SE and (c) EDS spectrum of BioC.

3.1.3.2. Ni/N-BioC

The SEM images of Ni/N-BioC are shown in Figure 10. It is possible to observe that this sample presents a roughened texture and that at lower magnification (5 000✕) the nickel particles are not clearly detected. To prove their presence SEM images were acquired at higher magnification (50 000✕) and EDS analysis was made. In Figure 10 (c) and (d) it is now possible to observe the nickel particles with different diameters. Two modes (mode SE and Z Cont) were made to better identify the nickel particles. Additionally, as expected, the EDS spectrum (Figure 10 (e)) shows the presence of carbon and nickel.
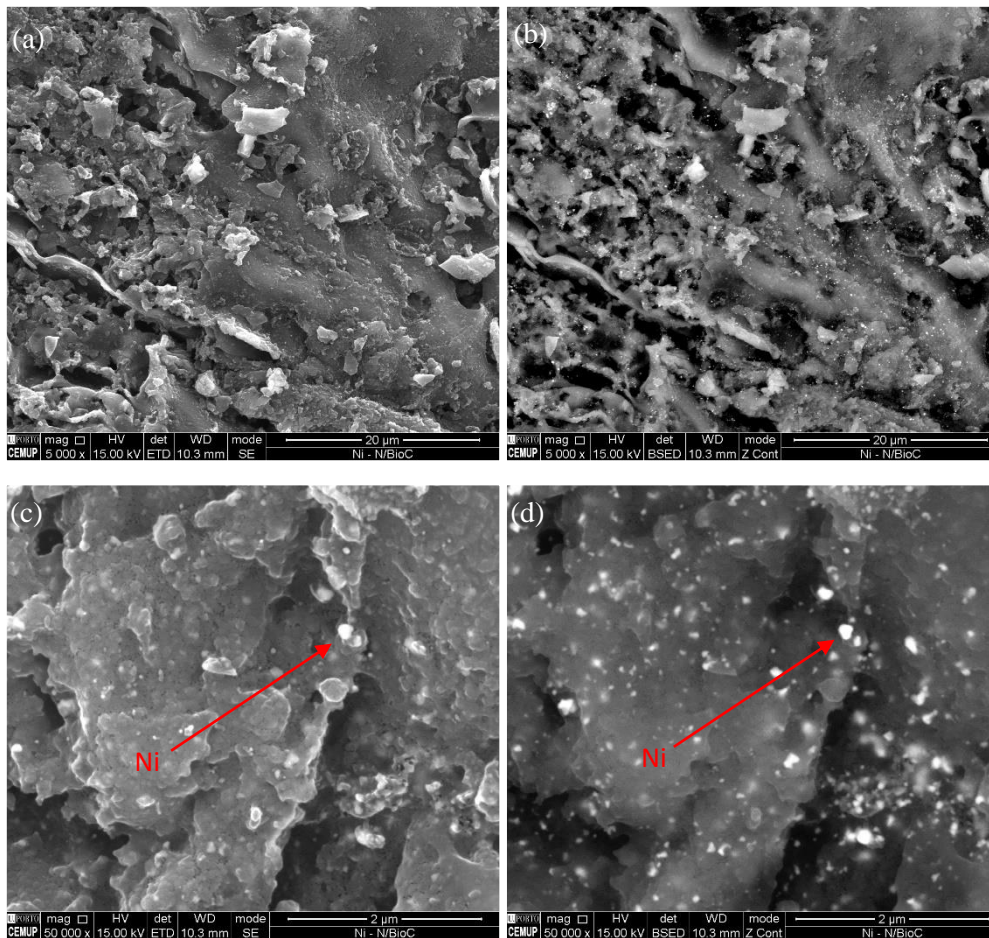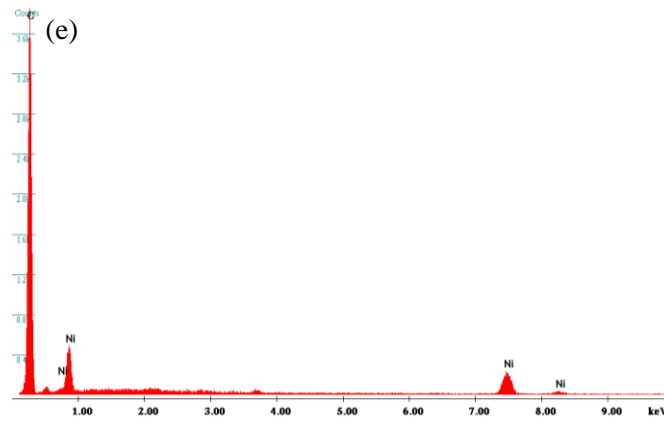
Figure 10 – (a) and (b) SEM images at magnification of 5 000× at mode SE and mode Z Cont, respectively, (c) and (d) SEM images at magnification of 50 000× at mode SE and Z Cont, respectively and (e) EDS spectrum of Ni/N-BioC.

3.1.3.3. Fe/N-BioC

Figure 11 (a) and (b), represent the Fe/N-BioC at a magnification at 5 000× at mode SE and mode Z Cont, respectively. Contrary to Ni/N-BioC sample, the iron particles are already observed at this magnification. Nevertheless, SEM images at higher magnification (50 000×) at mode SE and mode Z Cont were also made (Figure 11 (c) and (d)) which confirmed the presence of Fe particles and showed that these present different sizes. EDS further confirmed their presence as well as carbon, and oxygen.
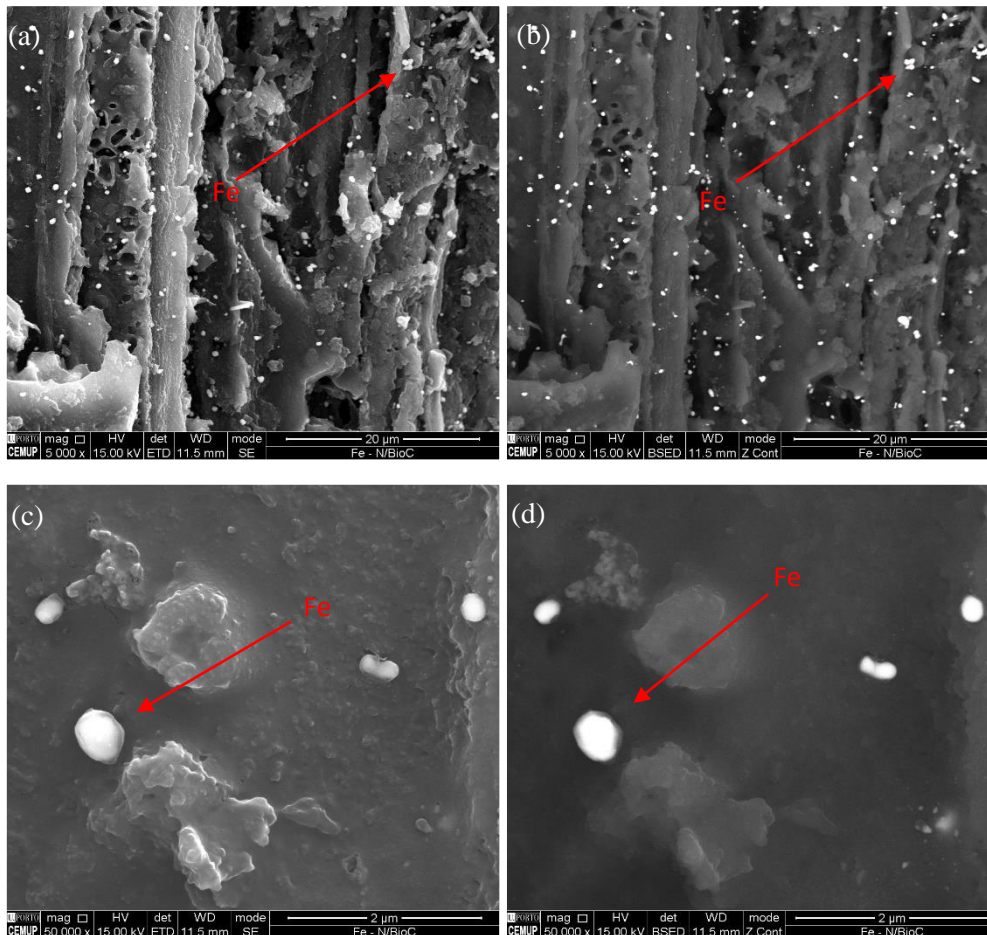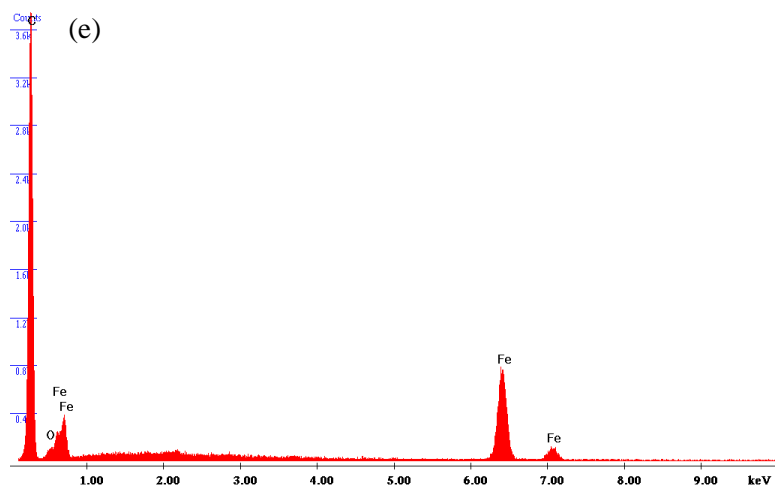
Figure 11 – (a) and (b) SEM images at magnification of 5 000× at mode SE and mode Z Cont, respectively, (c) and (d) SEM images of at magnification of 50 000× at mode SE and Z Cont, respectively and (e) EDS spectrum of Fe/N-BioC.

3.1.3.4. V/N-BioC

The presence of vanadium particles in V/N-BioC is clearly observed in Figure 12 (a) and (b). As for the other samples a roughened texture is observed and some agglomeration of vanadium particles is also detected (Figure 12 (c) and (d)). The EDS spectrum (Figure 12 (e)) shows the presence of carbon, oxygen, and vanadium.
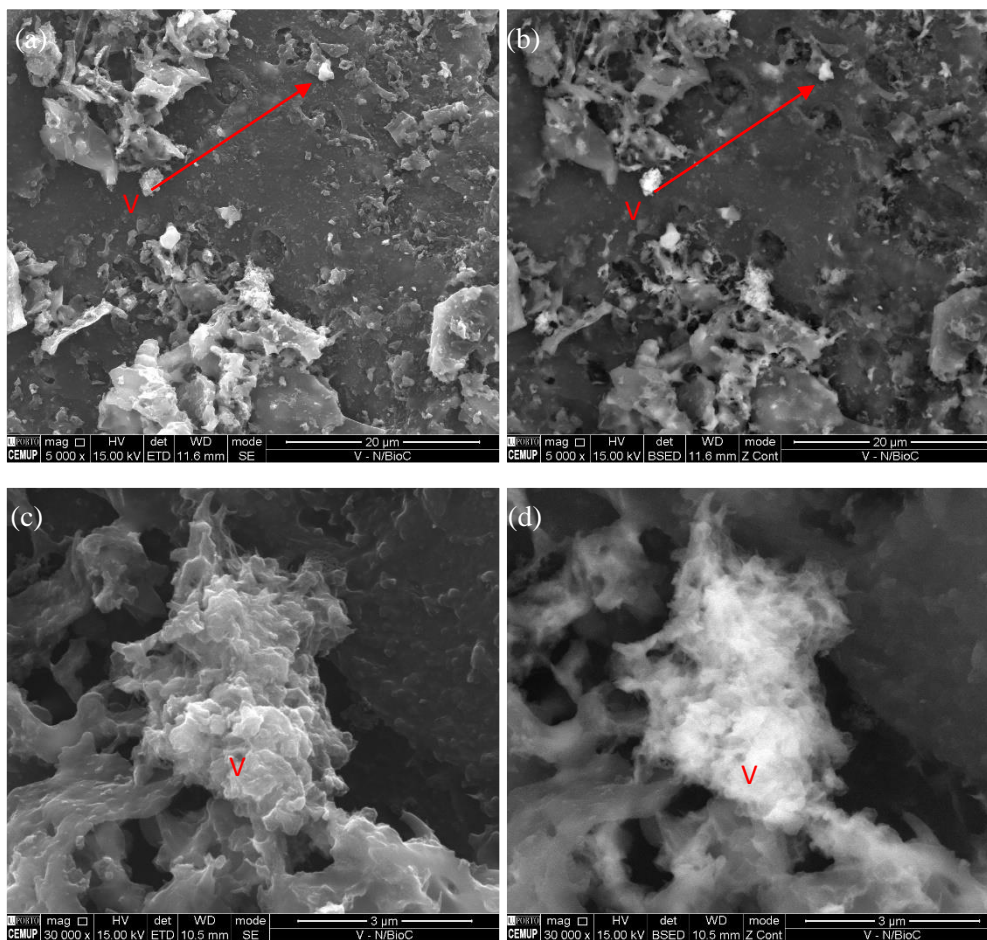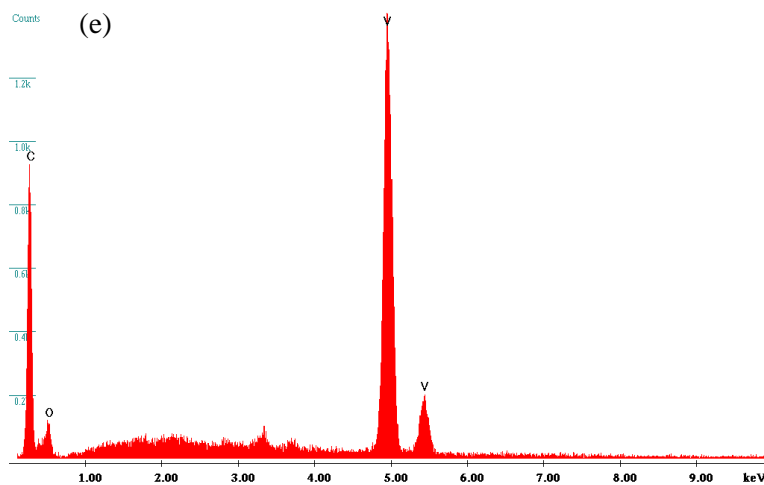
Figure 12 – (a) and (b) SEM images at magnification of 5 000× at mode SE and mode Z Cont, respectively, (c) and (d) SEM images of at magnification of 30 000× at mode SE and Z Cont, respectively and (e) EDS spectrum of V/N-BioC.

3.1.3.5. Cu/N-BioC

In Figure 13 (a) and (b), are represented the SEM images of Cu/N-BioC at a magnification of 5 000× at mode SE and mode Z Cont, respectively. It is possible to see the copper represented by the white dots in Figure 13 (b)). EDS analysis (Figure 13 (c)) confirmed the presence of copper as well as carbon and oxygen.
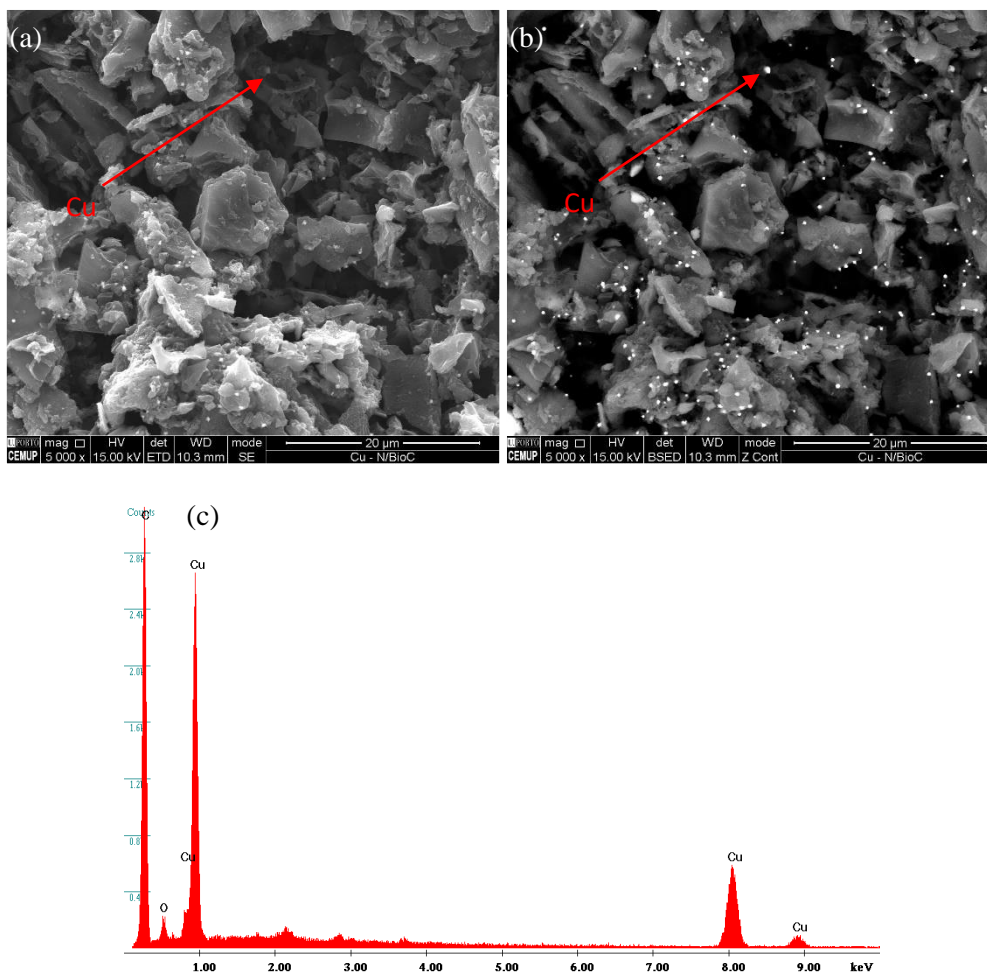
Figure 13 – (a) and (b) SEM images at magnification of 5 000× at mode SE and mode Z Cont, respectively, respectively and (c) EDS spectrum of Cu/N-BioC.

3.1.3.6. Zn/N-BioC

In Figure 14 (a) are depicted the SEM images of Zn/N-BioC at 5 000× and in Figure 14 (b) and (c), at 30 000× at mode SE and Z Cont, respectively. For this samples it was not clear the presence of the metal even at higher magnification. Nevertheless, the EDS spectrum (Figure 14 (d)) showed the presence of zinc as well as carbon, oxygen, and calcium which confirms the immobilization of the desired metal.
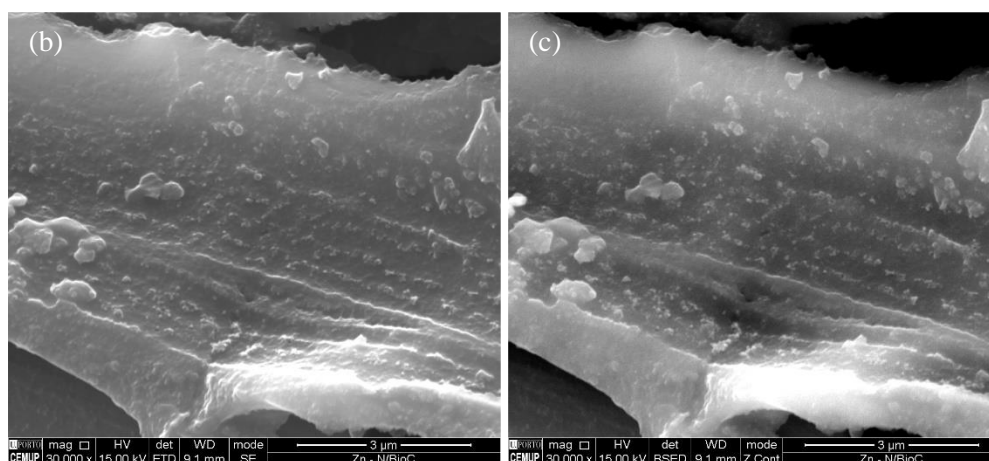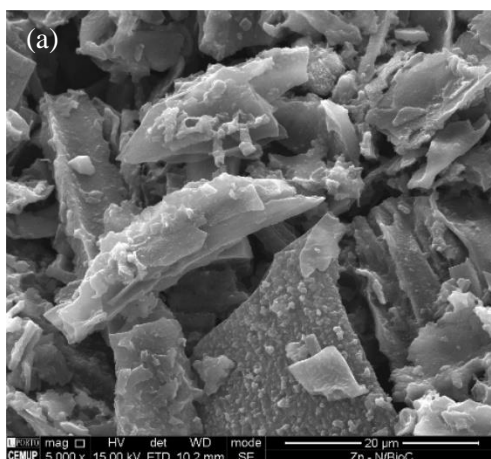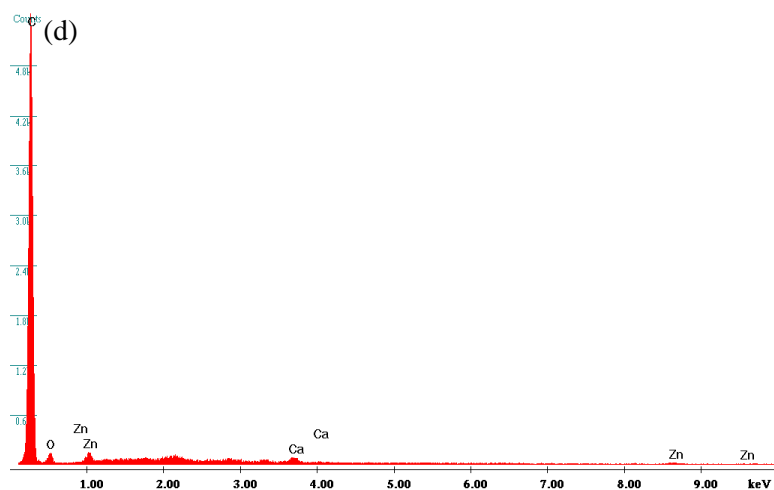
Figure 14 – (a) SEM images at magnification of 5 000✕, (b) and (c) SEM images at magnification of 30 000✕ at mode SE and mode Z Cont, respectively and (d) EDS spectrum of Zn/N-BioC.

3.1.3.7. Pd/N-BioC

The SEM images of Pd/N-BioC are depicted in Figure 15 (a) and (b), with a magnification of 5 000× and 30 000×, respectively. It is possible to see clusters of palladium particles in the two magnifications and in this case, they have similar diameters oppositely to what was observed for other metal particles. EDS spectrum (Figure 15 (c)) confirms the presence of carbon and palladium.
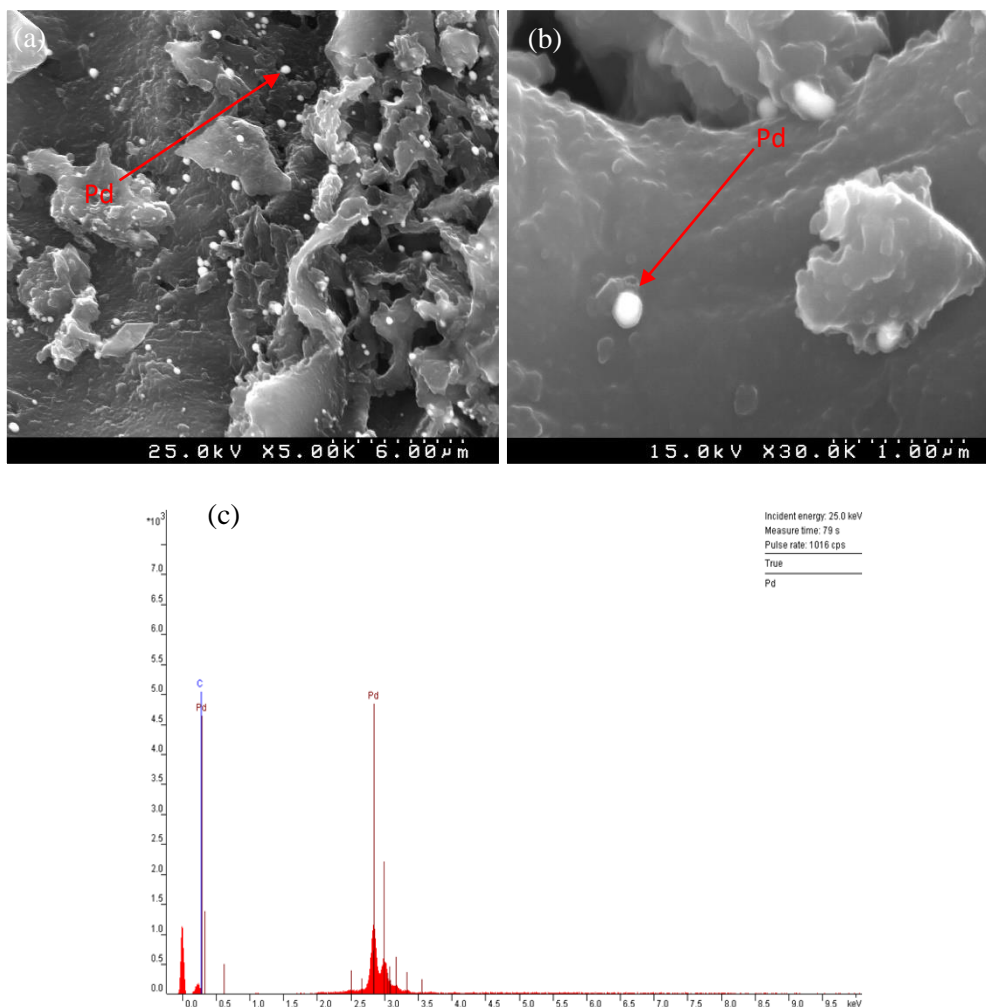
Figure 15 – (a) SEM images at magnification of 5 000×, (b) SEM images of at magnification of 30 000× and (c) EDS spectrum of Pd/N-BioC.

3.1.3.8. Co/N-BioC

The SEM images of Co/N-BioC are depicted in Figure 16 (a) and (b), with a magnification of 5 000× and 30 000×, respectively. It is possible to see a cobalt particle in figure 16 (b). The EDS spectrum (Figure 16 (c)) confirms the presence of carbon, nitrogen, and cobalt.
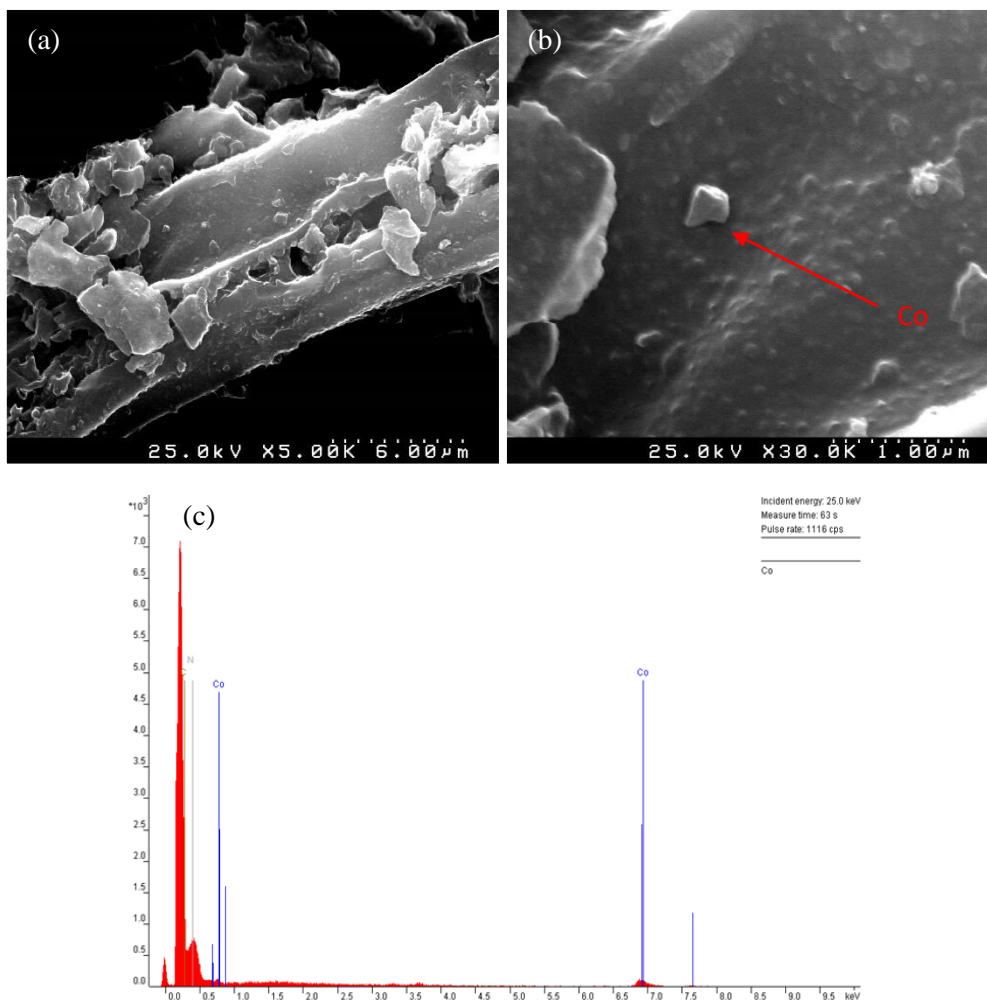
Figure 16 – (a) SEM images at magnification of 5 000×, (b) SEM images of at magnification of 30 000× and (c) EDS spectrum of Co/N-BioC.

3.1.3.9. Co,Ni/N-BioC

The SEM images of Co,Ni/N-BioC are depicted in Figure 17 (a) and (b), with a magnification of 5 000× and 30 000×, respectively. For this samples it was not clear the presence of the metals even at higher magnification. Nevertheless, the EDS spectrum (Figure 17 (c)) showed the presence of carbon, nitrogen, cobalt, nickel, and potassium which confirms the immobilization of the desired metals.
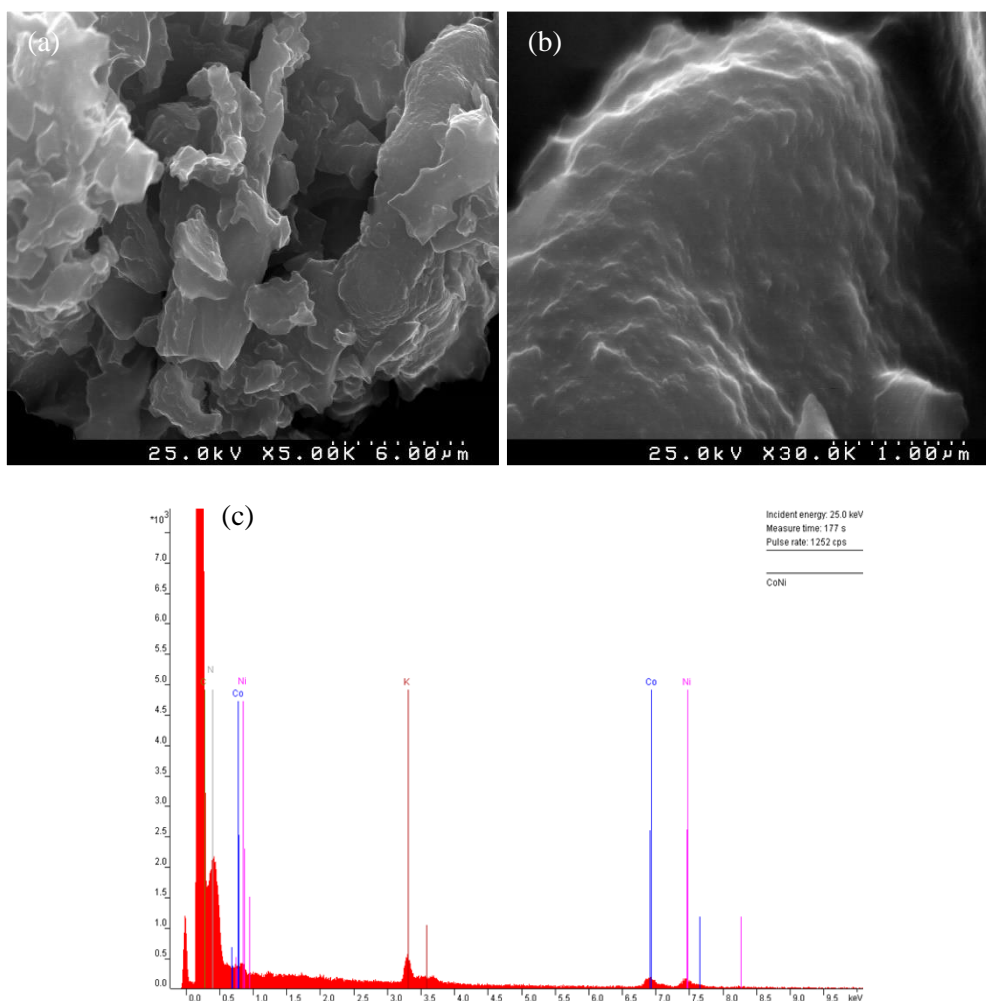
Figure 17 – (a) SEM images at magnification of 5 000×, (b) SEM images of at magnification of 30 000× and (c) EDS spectrum of Co,Ni/N-BioC.

3.1.4. X-ray Powder Diffraction (XRD)

The XRD patterns of unmodified BioC and all metal-supported BioC are shown in Figure 18. BioC is expected to be amorphous although some crystalline character may be present, as observed by the Bragg peaks (002), (100) and (110) at 2θ = 24.7 º, 43.1 º and 79.8 º (this is not well defined) revealing a crystallite orientation and size, Figure 18 (a). For Ni, Pd, Co and Cu diffraction peaks ascribed to the metal phase appear in the diffraction patterns of these catalysts which is indicative that these metals are in its reduced form. The XRD patterns of Ni/N-BioC presents the diffraction peaks at 2θ of 44.5º, 51.8º and 76.4º, corresponding, respectively, to the (111), (200) and (220) XRD crystal planes designated to the face-centered cubic crystallographic phase of metallic Ni (JCPDS data: 00-004-0850).[84]

The XRD patterns of Pd/N-BioC presents the diffraction peak at 2θ of 39.9º, 46.6º and 67.9º, corresponding to the (111), (200) and (220). (JCPDS data: 00-005-0681). [85, 86]

The XRD patterns of Co/N-BioC presents the diffraction peaks at 2θ of 44.2º, 51.5º and 75.9º, due to the (111), (200) and (220) planes attributed to the crystal faces of metallic Co (JCPDS data: 00-001-1255). [87, 88]

The XRD patterns of Cu/N-BioC presents the diffraction peak at 2θ 43.2º, 50.3º and 74.1º, corresponding to the (111), (200) and (220) XRD crystal planes of metallic copper (JCPDS data: 01-085-1326). [89, 90]

The XRD diffractograms of Fe/N-BioC and Zn/N-BioC are also presented in Figure 18. For Fe/N-BioC it was not possible to make a right attribution due to the small peaks intensity, however it presents a profile very similar to the phase of Fe_3C (JCPDS data: 35-0772). [91] In the case of Zn/N-BioC, it wasn't possible to detect diffraction peaks besides the diffraction peaks from biochar and this could be due to the low Zn concentration in biochar observed in ICP-OES and in the SEM images, see Figures 8 and 14. The XRD patterns of V/N-BioC presents the diffraction peaks at 2θ of 37.6º, 43.7º and 63.7º attributed to vanadium(III) oxide (V_2O_3). (JCPDS data: 01-075-0048). [92]
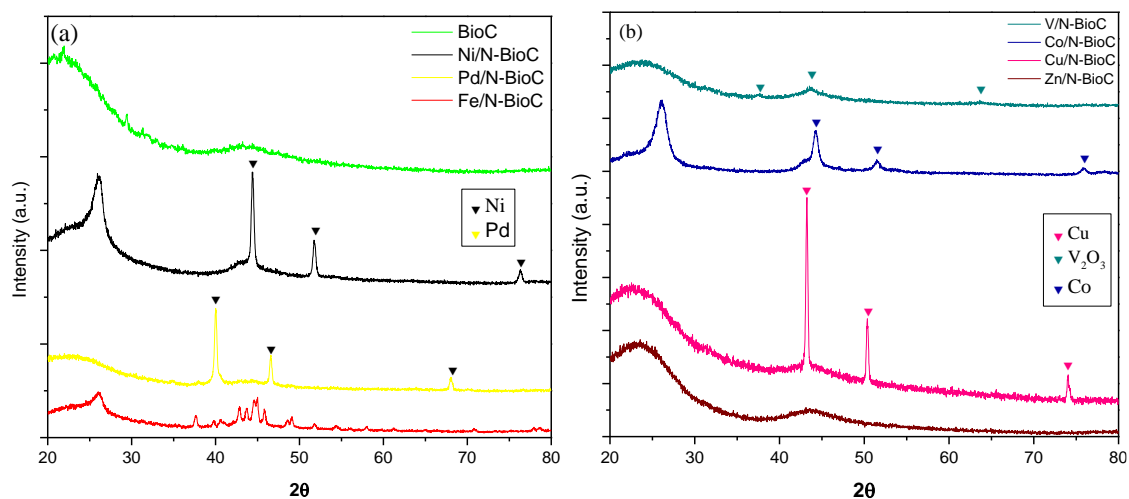
Figure 18 – XRD spectra of (a) BioC, Ni/N-BioC, Pd/N-BioC, Fe/N-BioC and (b) V/N-BioC, Co/N-BioC, Cu/N-BioC and Zn/N-BioC.

3.2.   Electrocatalytic performance towards ORR

The ORR electrocatalytic performance of all materials prepared was initially assessed by cyclic voltammetry. Figures 19 (a-k) show the results for all the materials prepared (BioC, N/S-BioC, N-BioC, Ni/N-BioC, Pd/N-BioC, Fe/N-BioC, V/N-BioC, Co/N-BioC, Cu/N-B Zn/N-BioC and Co,Ni/N-BioC). For comparison, Pt/C was also tested in the same experimental conditions and the CVs can be observed in Figure 19 (l).

In N_2-saturated electrolyte most of the materials prepared did not show electrochemical processes in the potential range used oppositely to Co/N-BioC which showed a pair of redox peaks (E_{pc} = 1.02 and E_{pa} = 1.12 V vs RHE) corresponding to the reduction/oxidation of cobalt. In contrast, in the presence of O_2, all the materials presented an irreversible ORR peak at E_{pc} = 0.66, 0.56, 0.56, 0.72, 0.64, 0.76, 0.73, 0.81, 0.50, 0.65 and 0.75 V vs. RHE for BioC, N/S-BioC, N-BioC, Ni/N-BioC, Pd/N-BioC, Fe/N-BioC, V/N-BioC, Co/N-BioC, Cu/N-BioC, Zn/N-BioC and Co,Ni/N-BioC, respectively. In the same experimental conditions, Pt/C (20 wt %), showed the ORR peak at E_{pc} = 0.86 V vs. RHE.
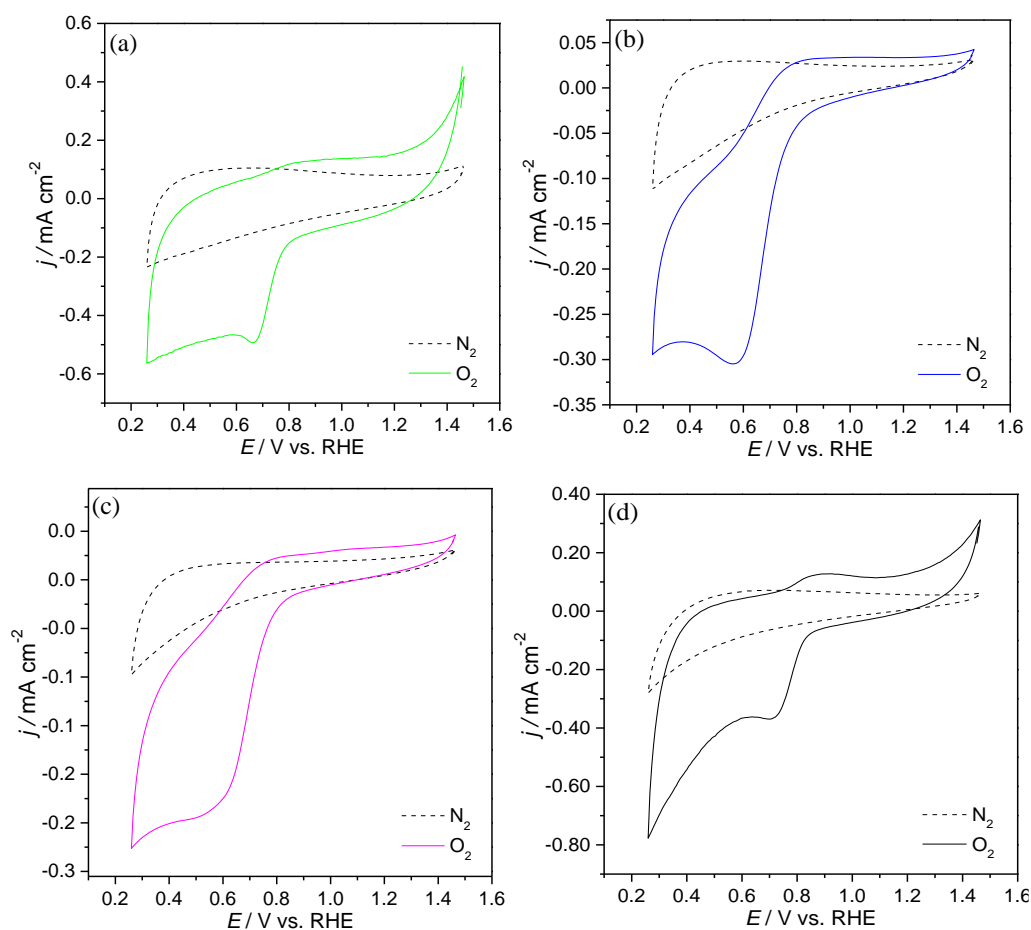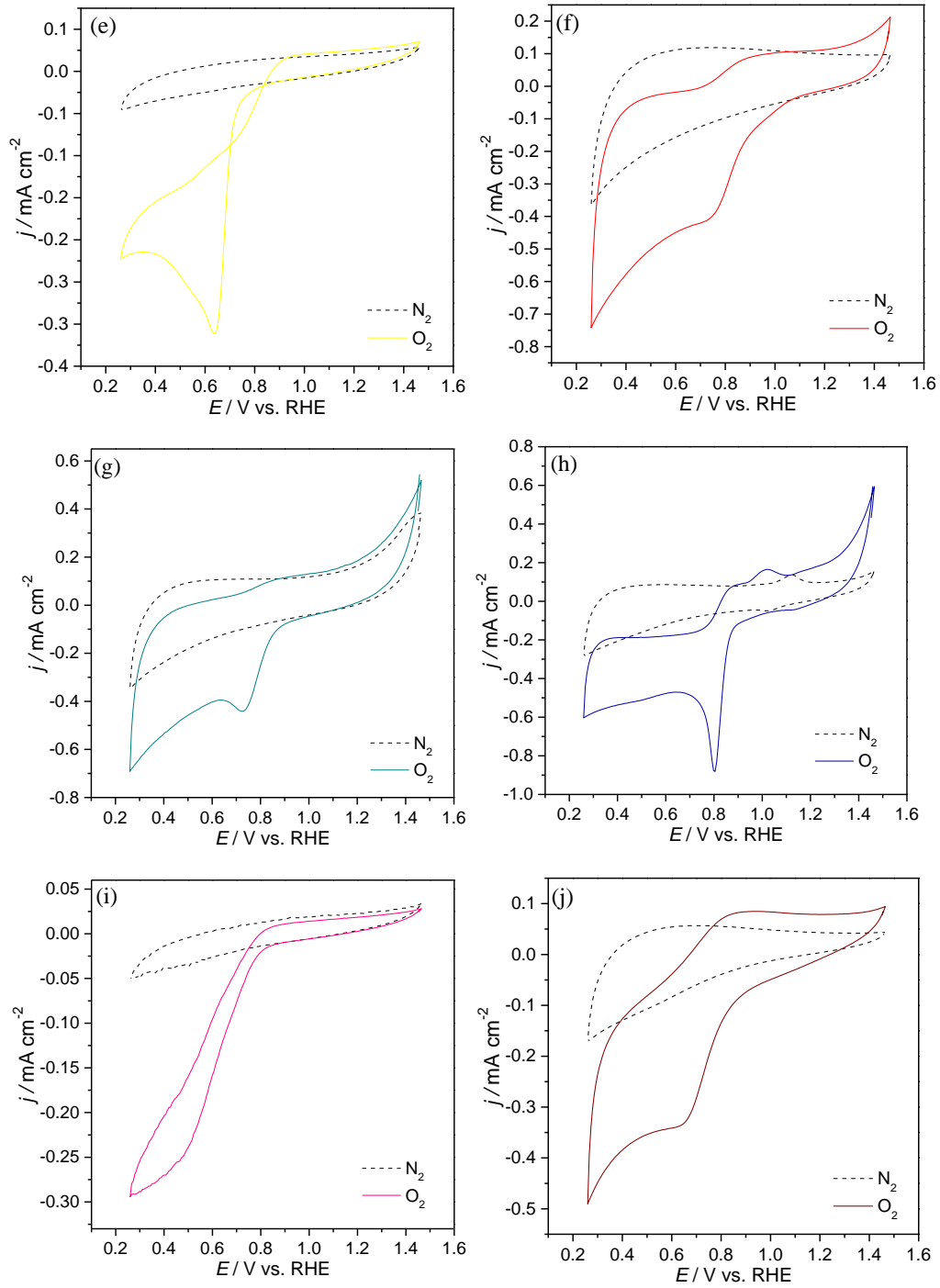
Figure 19 – CVs of (a) BioC, (b) N/S-BioC, (c) N-BioC, (d) Ni/N-BioC, (e) Pd/N-BioC, (f) Fe/N-BioC, (g) V/N-BioC, (h) Co/N-BioC, (i) Cu/N-BioC, (j) Zn/N-BioC, (k) Co,Ni/N-BioC and (l) Pt/C, modified RDE in N_2-satured (dash line) and O_2-satured (full line) 0.1 mol dm^{-3} KOH solution at 0.005 V s^{-1}.

To unveil the kinetics of the oxygen reduction reaction, linear sweep voltammetry was performed in N_2- and O_2-saturated KOH solution (0.1 mol dm^{-3}) at different rotation speeds (400 − 3000 rpm). Figures 20 (a-k) show the LSV for all the materials prepared while the results for Pt/C are depicted in Figure 20 (l). The ORR activity parameters (E_{onset}, j_L and n_{O2}) were obtained from LSV curves and are presented in Table 4.

All electrocatalysts presented a linear increase in the j_L values as the rotation speed increased indicating that the electron transfer reaction is diffusion limited.[93] The LSVs of the ECs tested showed two or three distinct regions. For example, for Pt/C in Figure 20 (l), for potential values more positive than $E \approx 0.90$ V vs. RHE there is a plateau, and the ORR is kinetically controlled. In the region between $E \approx 0.90$ V and $E \approx 0.65$ V vs. RHE there is a mixed kinetic-diffusion region, and for potential values more negative than $E \approx 0.65$ V vs. RHE the ORR is controlled by the diffusion of oxygen.[94] However, the same behaviour is not observed for most of the electrocatalysts prepared as only for Co/N-BioC and Pd/N-BioC these three regions can be clearly distinguished. Still, for simplicity the last j value obtained in the potential window studied will be assumed throughout this thesis as the diffusion-limiting current density value (j_L, 0.26V, 1600 rpm).

All metal-containing ECs presented higher onset potential values (0.88 V ≥ E_{onset} ≥ 0.76 V) than the pristine BioC (0.76 V) and doped BioC (0.71 V) except for Cu/N-BioC (0.66 V) suggesting that metal incorporation contributes to the improvement of ORR performance. The highest E_{onset} value were obtained for Co/N-BioC and Fe/N-BioC which was only 0.06 and 0.07 V lower than that obtained for the state-of-the-art Pt/C (0.94 V). Higher j_L values were also obtained for Co/N-BioC (-3.48 mA cm^{-2}) and Fe/N-BioC (-3.24 mA cm^{-2}) followed by Ni/N-BioC (-2.78 mA cm^{-2}) and V/N-BioC (-2.74 mA cm^{-2}). The other ECs presented values between -2.39 and -1.27 mA cm^{-2}. Even though the value obtained for Co/N-BioC is good it is still somewhat far from that obtained for Pt/C (-4.68 mA cm^{-2}). The good ORR performance of Co/N-BioC can be attributed to the synergistic effect arising from the N-doped and cobalt in biochar. [95]
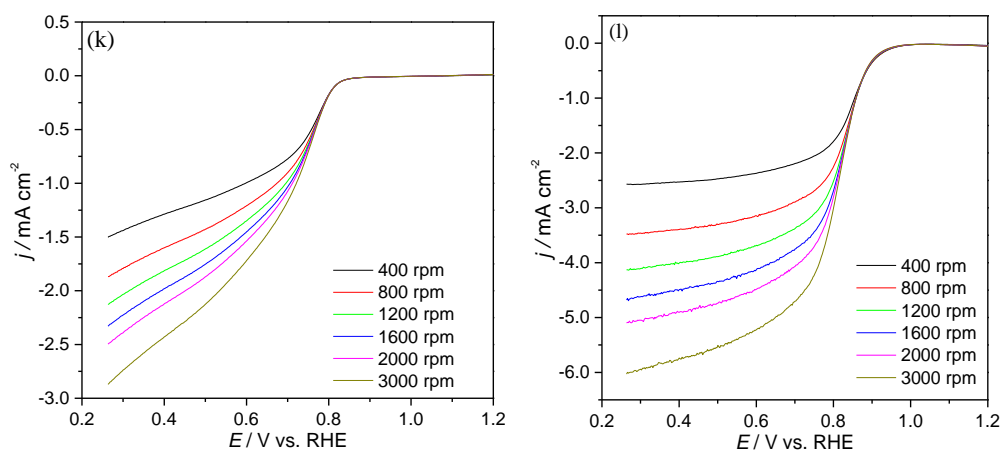
Figure 20 – LSVs of (a) BioC, (b)N/S-BioC, (c) N-BioC, (d) Ni/N-BioC, (e) Pd/N-BioC, (f) Fe/N-BioC, (g) V/N-BioC, (h) Co/N-BioC, (i) Cu/N-BioC, (j) Zn/N-BioC, (k) Co,Ni-BioC and (l) Pt/C at different rotation rates in O$_2$-satured KOH solution at 0.005 V s^{-1}.

The ORR kinetic parameters were then evaluated using the Koutecky-Levich (K-L) plots, which were acquired from LSVs at different rotating speeds. Figures 21 (a-k) show the K-L plots for all material prepared, while that corresponding to Pt/C is depicted in Figure 21 (l). All ECs presented a linear relationship between j^{-1} vs. $\omega^{-1/2}$ (K-L plots) suggesting a first order electrocatalytic ORR with respect to the concentration of dissolved O$_2$. In addition, the slopes of the K-L plots of BioC, N/S-BioC, N-BioC, Ni/N-BioC, Pd/N-BioC, Fe/N-BioC, V/N-BioC, Co/N-BioC, Cu/N-BioC, Zn/N-BioC and Co,Ni/N-BioC are 10.56 – 13.05, 10.52 – 11.75, 12.10 – 14.41, 11.22 – 13.63, 11.20 – 12.20, 7.77 – 8.27, 10.0 – 12.45, 7.85 – 8.90, 11.79 – 10.58 12.10 – 13.63, and 9.91 – 11.57, respectively. This suggests a dependency of the number of transferred electrons per oxygen molecule with the potential.
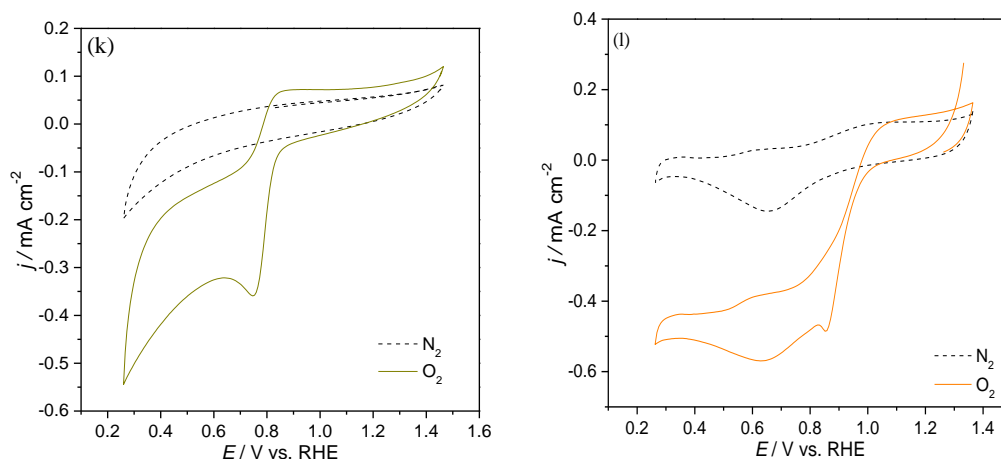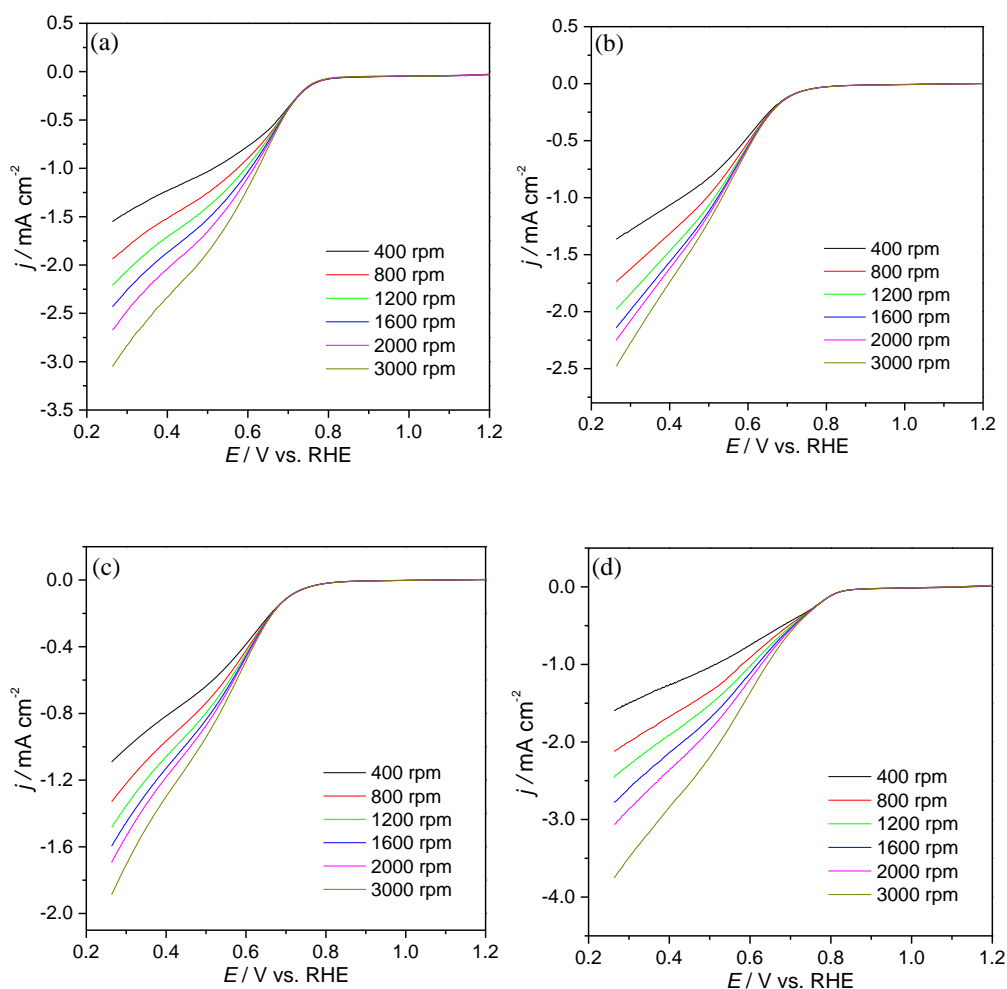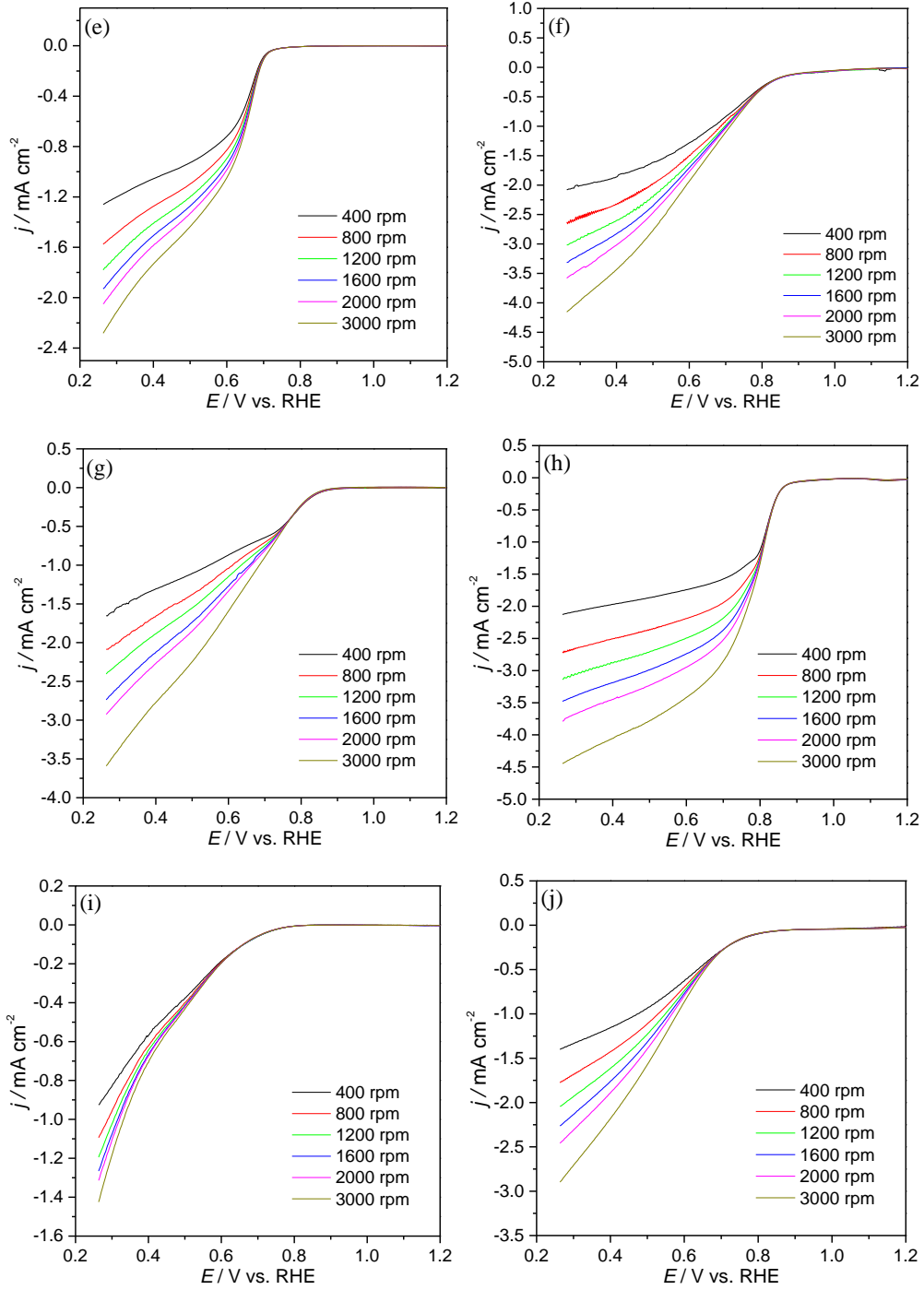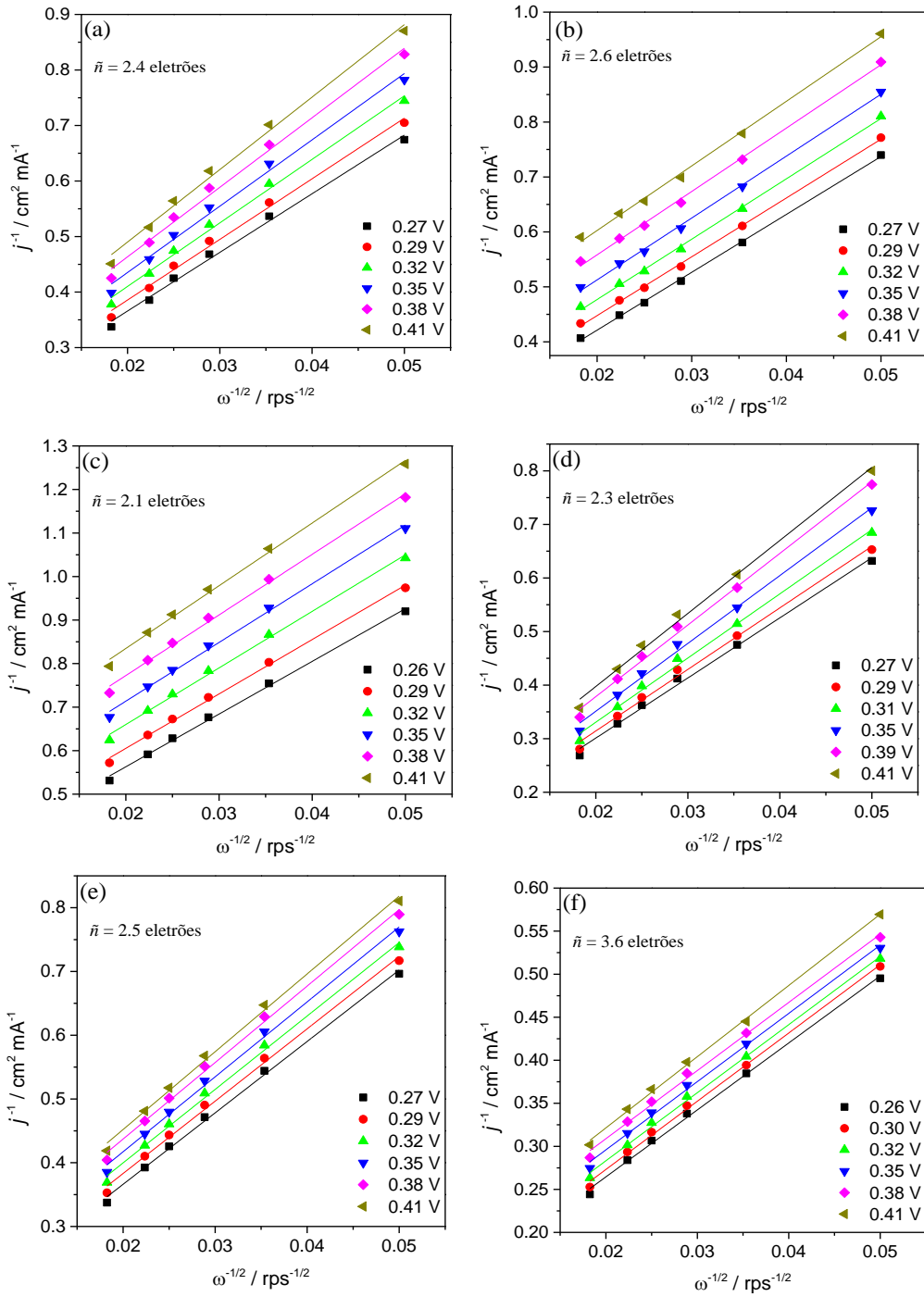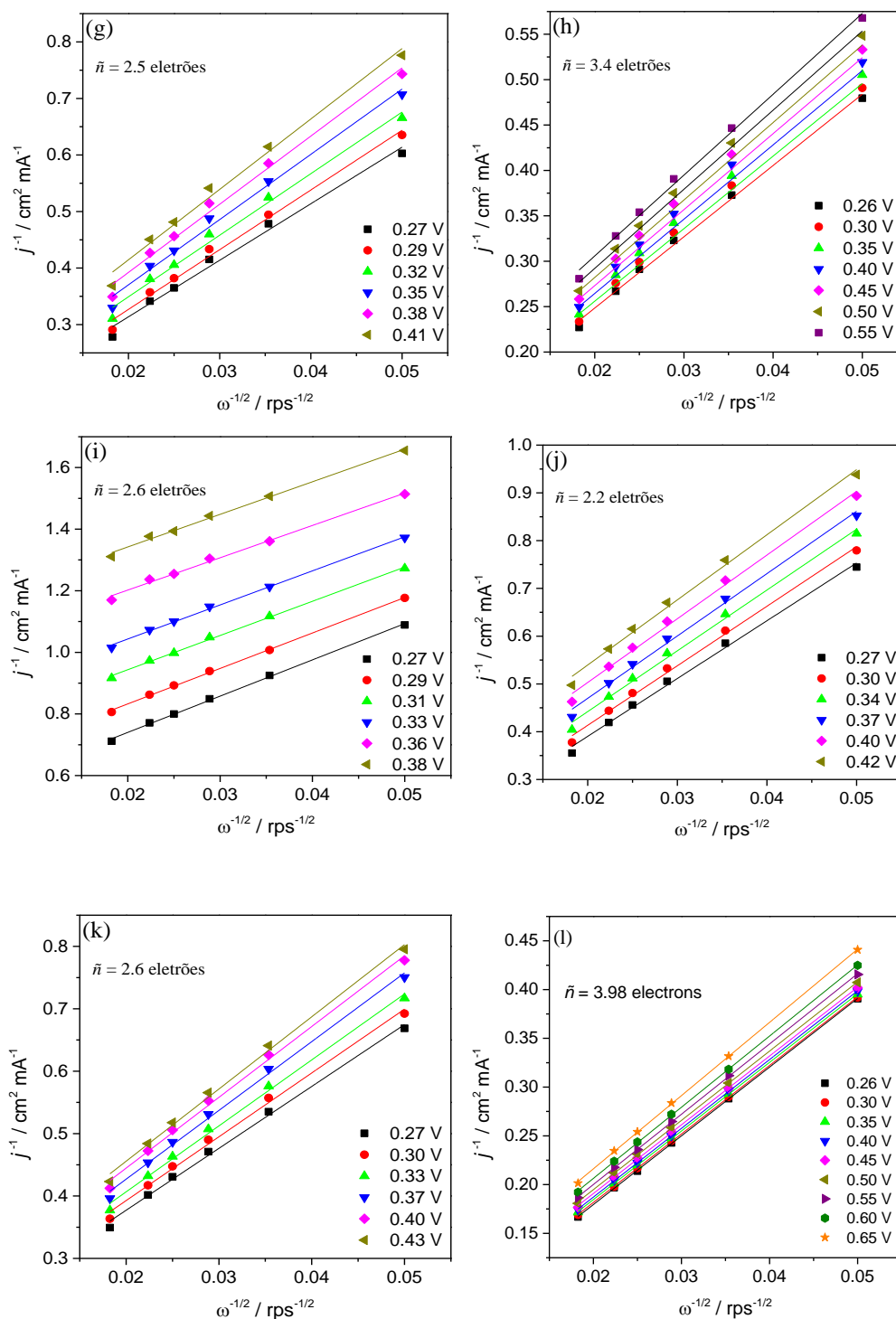
Figure 21 – Koutecky-Levich (K-L) plots of (a) BioC, (b)N/S-BioC, (c) N-BioC, (d) Ni/N-BioC, (e) Pd/N-BioC, (f) Fe/N-BioC, (g) V/N-BioC, (h) Co/N-BioC, (i) Cu/N-BioC, (j) Zn/N-BioC, (k) Co,Ni/N-BioC and (l) Pt/C.

The n_{O2} values were estimated by the K-L equation. The n_{O2} values increased as the potential decreases from 0.55 to 0.27 V vs. RHE: 2.17 – 2.68, 2.41 – 2.69, 1.97 – 2.34, 2.08 – 2.53, 2.32 – 2.53, 3.43 – 3.64, 2.28 – 2.84, 3.18 – 3.55, 2.08 – 2.34 and 2.50 – 2.86 electrons, for BioC, N/S-BioC, N-BioC, Ni/N-BioC, Pd/N-BioC, Fe/N-BioC, V/N-BioC, Co/N-BioC, Zn/N-BioC and Co,Ni/N-BioC, respectively. Oppositely, the n_{O2} of Cu/N-BioC decreases from 2.68 – 2.41 electrons from 0.38 to 0.27 V vs. RHE. These results suggest that in the potential range scanned, BioC, N-BioC, Ni/N-BioC and Zn/N-BioC are involved in a 2-electron process. N/S-BioC, Pd/N-BioC, V/N-BioC, Cu/N-BioC and Co,Ni/N-BioC are involved in a mixed-regime mechanism of 2- and 4-electron, since the n_{O2} values are close to 3 electrons. Finally, Fe/N-BioC and Co/N-BioC are closer to the direct 4-electron mechanism with n_{O2} values of 3.6 and 3.4, respectively.

The LSV curves of all ECs tested at 1600 rpm are depicted in Figure 22 (a) while the n_{O2} values in the potential range from 0.25 to 0.50 V vs. RHE in Figure 22 (b) to better see the results obtained and, as discussed above, it is clear that Co/N-BioC and Fe/N-BioC present the best results even though their performance is still somewhat far from that for Pt/C. In Figure 22 (c) are depicted the Tafel plots for all the ECs tested and these were obtained from the LSV data in Figure 22 (a).
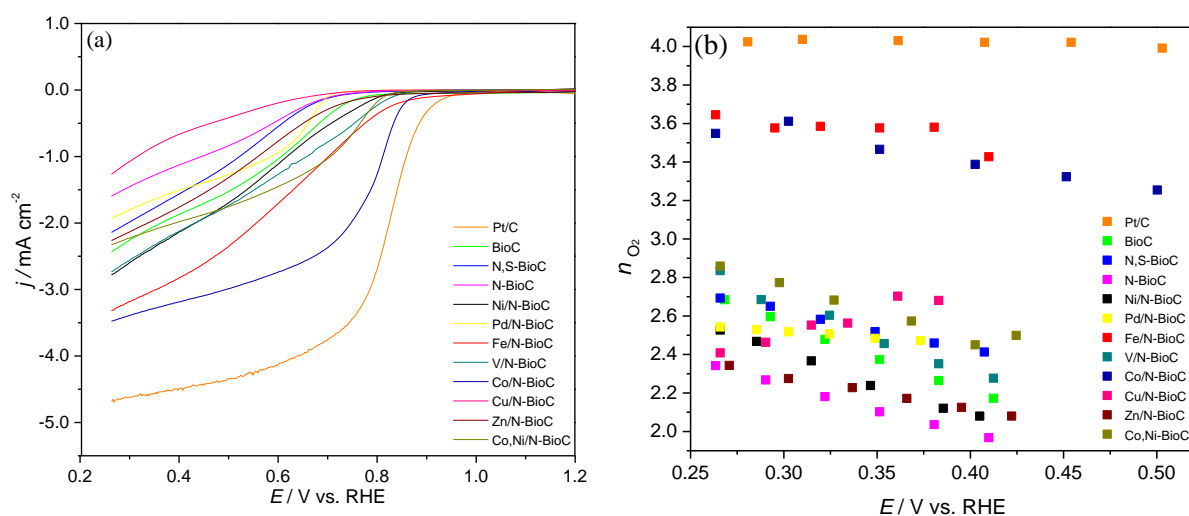
Figure 22 – (a) ORR LSV curves of Pt/C, BioC, N/S-BioC, N-BioC, Ni/N-BioC, Pd/N-BioC, Fe/N-BioC, V/N-BioC, Co/N-BioC, Cu/N-BioC, Zn/N-BioC and Co,Ni-BioC acquired in O_2-saturated KOH solution 0.1 mol dm^{-3} at 1600 rpm and 0.005 V s^{-1}; (b) n_{O2} at several potential values and (c) the respective ORR Tafel plots.

The ORR process exhibits Tafel slopes of 131, 142, 136, 103, 124, 181, 67, 61, 162, 202 and 62 mV dec^{-1} for BioC, N/S-BioC, N-BioC, Ni/N-BioC, Pd/N-BioC, Fe/N-BioC, V/N-BioC, Co/N-BioC, Cu/N-BioC, Zn/N-BioC and Co,Ni/N-BioC, respectively. For Pt/C the slope obtained was 88.6 mV dec^{-1}. Tafel slope values between 88.6 and 202 mV dec^{-1} suggest that for these electrocatalysts the reaction rate is determined by the first discharge step or the upon consumption of the MOOH species with high coverage of MOO$^-$ (where M is an empty site on the electrocatalyst surface).[96] On the other hand, the Tafel slope values close to 60 mV dec^{-1} obtained for V/N-BioC (67 mV dec^{-1}), Co/N-BioC (61.4 mV dec^{-1}) and Co,Ni/N-BioC (62 mV dec^{-1}), anticipate a mechanism where the overall reaction rate is determined by the elementary step of conversion of the intermediate surface adsorbed specie MOO$^-$ to MOOH. Also, the lower Tafel slopes comparing to Pt/C, suggests that these two BioC can easily adsorb O_2 onto their surface and activate it, promoting a robust electrocatalytic performance towards ORR. [13, 94]

Table 4 – ORR activity parameters: Onset potentials (E_{onset}), diffusion-limiting current density (j_L, 0.26 V, 1600 rpm), number of electrons transferred per O_2 molecule (n_{O2}) and Tafel slope values derived from the ORR polarization curves in O_2-satured 0.1 mol dm^{-3} KOH solution for Pt/C and BioC, N/S-BioC, N-BioC, Ni/N-BioC, Pd/N-BioC, Fe/N-BioC, V/N-BioC, Co/N-BioC, Cu/N-BioC, Zn/N-BioC and Co,Ni/N-BioC.

Sample	E_{onset} (V vs. RHE) (5%Total)	E_{onset} (V vs. RHE) (j=0.1 mA cm^{-2})	j_L (mA cm^{-2})	n_{O2}	Tafel slope (mV dec^{-1})
Pt/C	0.91	0.94	-4.68	3.9	89
BioC	0.77	0.76	-2.39	2.4	131
N,S-BioC	0.71	0.71	-2.14	2.6	142
N-BioC	0.72	0.71	-1.60	2.1	136
Ni/N-BioC	0.79	0.81	-2.78	2.3	103
Pd/N-BioC	0.78	0.78	-1.93	2.5	124
Fe/N-BioC	0.88	0.85	-3.24	3.6	181
V/N-BioC	0.82	0.83	-2.74	2.5	67
Co/N-BioC	0.86	0.88	-3.48	3.4	61
Cu/N-BioC	0.70	0.66	-1.27	2.6	162
Zn/N-BioC	0.78	0.76	-2.20	2.2	202
Co,Ni/N-BioC	0.81	0.82	-2.33	2.6	62

The ORR mechanistic pathways were also explored through the RRDE measurements. An alternative to the traditionally used process for producing H_2O_2, is via the two-electron oxygen electrochemical reaction. This process has high selectivity, activity and stability.[97] The estimated percentage of H_2O_2 produced for each modified electrode was calculated through Eq. (4) and is presented in Figure 23 at several potential values. The lowest percentage of H_2O_2 ($\approx$ 25%) was obtained for Fe/N-BioC and Co/N-BioC which is in accordance with the highest $ñ_{O2}$ values obtained of n_{O2}=3.6 and 3.4, for Fe/N-BioC and Co/N-BioC, respectively. For Pd/N-BioC, V/N-BioC, N,S-BioC, Co,Ni/N-BioC and Cu/N-BioC the values were intermediates ($\approx$ 41–60%) suggesting a mixed regime mechanism of 2$^-$ and 4$^-$ electrons as predicted from the K–L plots, with n_{O2} values between 2.5 and 2.6. For N-BioC, Zn/N-BioC, Ni/N-BioC and BioC the values were higher ($\approx$ 53–75%) suggesting a mechanism of 2$^-$ electrons, in accordance with the obtained n_{O2} values (2.1–2.4 electrons).
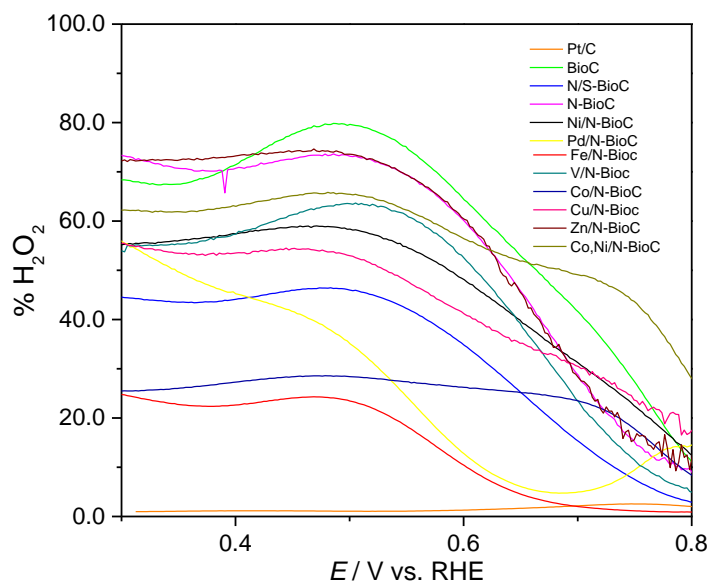
Figure 23 – Estimated percentage of H$_2$O$_2$ formed of the Pt/C, BioC, N/S-BioC, N-BioC, Ni/N-BioC, Pd/N-BioC, Fe/N-BioC, V/N-BioC, Co/N-BioC, Cu/N-BioC, Zn/N-BioC and Co,Ni/N-BioC.

Electrocatalyst presenting good performance towards ORR should exhibit good tolerance to methanol because, in fuel cells, the methanol crossover from the anode to the cathode can reduce the cathodic performance, if the electrocatalyst is sensitive to it.[13] Therefore, the effect of methanol was evaluated by chronoamperometry in O$_2$-saturated 0.1 mol dm^{-3} KOH to which was added 0.5 mol dm^{-3} of methanol at $t \approx 500$ s and the results can be observed in Figure 24. For Pt/C, the addition of methanol causes a current decrease to $\approx$ 51% of its initial current which confirms one of the disadvantages of Pt/C electrocatalyst. The BioC is also sensitive to methanol which causes a current decrease to 62%. The remaining biochar materials retained between 78 to 97% of their initial current, suggesting a good selectivity towards ORR and the good tolerance towards crossover methanol effect. The best tolerance to methanol was achieved for Ni/N-BioC (97%), followed by Co/N-BioC (93%) and Fe/N-BioC (91%). These results establish that the ECs are promising for ORR, overcoming an inherent problem of Pt-based ORR electrocatalysts.

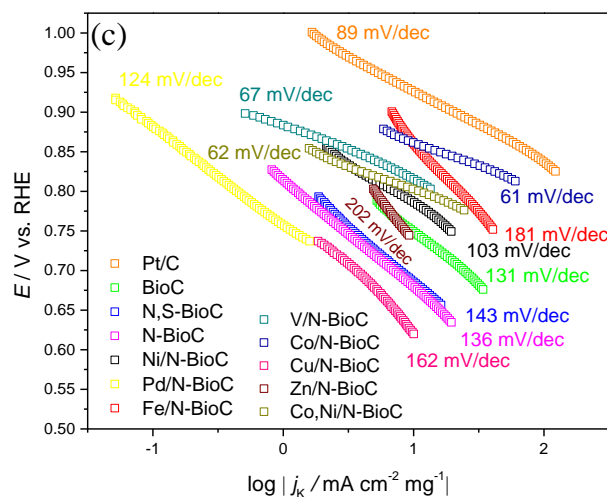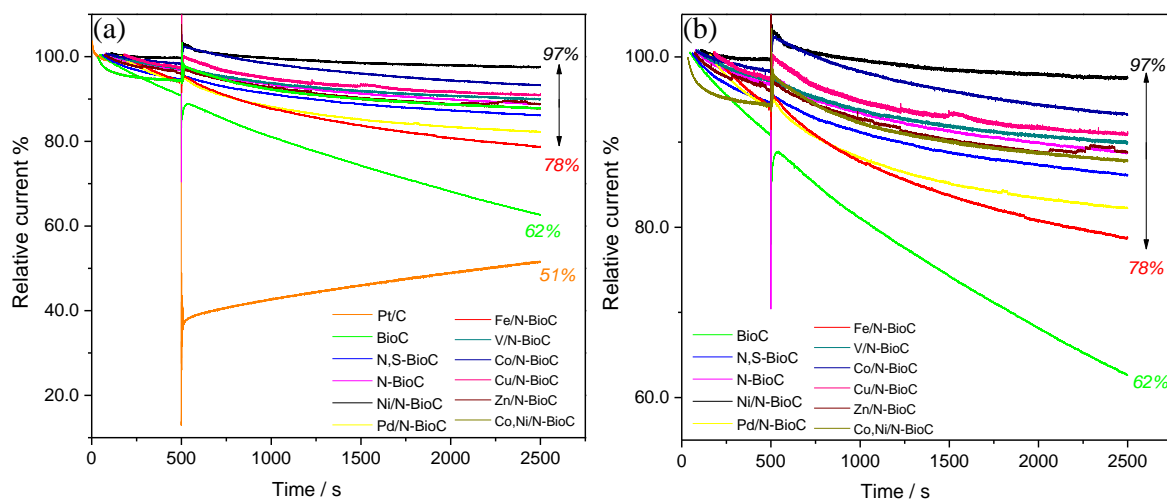Figure 24 – (a) Chronoamperometric responses of the Pt/C, BioC, N/S-BioC, N-BioC, Ni/N-BioC, Pd/N-BioC, Fe/N-BioC, V/N-BioC, Co/N-BioC, Cu/N-BioC, Zn/N-BioC and Co,Ni/N-BioC with the addition of 0.5 mol dm^{-3} methanol after ≈500 s, at E=0.50 V vs. RHE, at 1600 rpm, in O_2-saturated KOH 0.1 mol dm^{-1}, and (b) a closer up of BioCs (without Pt/C).

Another extremely important parameter to evaluate is the electrocatalysts stability. This was evaluated by chronoamperometry at E = 0.50 V vs. RHE during 20 000 s at 1600 rpm. Figure 25 collects the chronoamperometric responses of Pt/C and all studied biochar materials. For Pt/C can be noted a small current decline to 89% while for the biochar-based electrocatalysts the current retention values varied between 53 and 83%. Co,Ni/N-BioC showed the best stability among the biochar-based materials with a current retention of 83% followed by Zn/N-BioC with 81%. It is important to notice that these values are only 6 and 8% lower than that obtained for Pt/C. This very small difference suggests a good long-term stability for these two biochars. Contrary to what was expected, Co/N-BioC lost 30% of its initial current after 20 000 s.
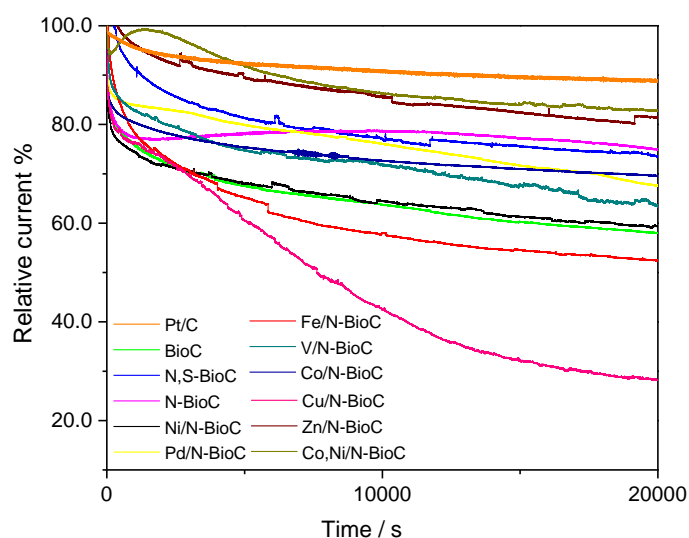
Figure 25 – Chronoamperometric responses of the of the Pt/C, BioC, N/S-BioC, N-BioC, Ni/N-BioC, Pd/N-BioC, Fe/N-BioC, V/N-BioC, Co/N-BioC, Cu/N-BioC, Zn/N-BioC and Co,Ni/N-BioC at E=0.50 V vs. RHE, at 1600 rpm, in O$_2$-saturated KOH (0.1 mol dm^{-3}) for 20 000 s.

Overall, the Co/N-BioC electrocatalyst presented the best ORR performance among the biochar-based materials evaluated. Still, comparing with other cobalt-containing electrocatalysts from literature (Table 5) some further improvements are needed. However, it is worth to mention that most of them are based in materials produced from petrochemical products via energy-intensive or harsh synthetic processes (graphene oxide, graphene, carbon nanotubes). Additionally, all these materials cannot be directly compared as they present different amounts of active sites like nitrogen and cobalt species. Also, the type of nitrogen, which is extremely important for electrocatalytic tests, was not determined due to the impossibility to analyse our samples by XPS.

Table 5 – Comparison of ORR activity parameters for different cobalt carbon materials doped with nitrogen.

Sample	E_{onset} (V vs. RHE)	n_{O2}	TS (mV dec^{-1})	Methanol	Stability	Ref.
Co/N-BioC	0.88	3.40	61	93	70	This work
Co/N-C-800	0.74	3.95	61	~100	96	[95]
Co@NC$_{BC}$	0.98	3.95	59	97	98	[98]
Co SAs/N-C(800)	0.86	~3.97	79	-	~100	[99]
Co/N-CNTs	0.94	3.90	50	~100	96.8	[100]
N/Co-doped PCP//NRGO	0.97	~3.92	85	98	85.6	[101]
CF-NG-Co	0.97	~3.9	44	~100	~100	[102]
Co-N-CNT frameworks	0.97	3.97	64	~100	96	[103]

3.3. Electrocatalytic performance towards OER

To evaluate the OER electrocatalytic performance of all materials prepared, LSV was performed in N_2-saturated KOH (0.1 mol dm^{-3}). In Figure 26 (a) are presented the OER polarization curves for BioC, N/S-BioC, N-BioC, Ni/N-BioC, Pd/N-BioC, Fe/N-BioC, V/N-BioC, Co/N-BioC, Cu/N-BioC, Zn/N-BioC and Co,Ni/N-BioC. The results are compared with state-of-the-art OER electrocatalysts, RuO_2 and IrO_2. Figure 26 (b) shows the results for electrocatalyst with the worst performance which cannot be distinguished in Figure 26 (a). The important OER parameters that can be obtained from the analysis of the LSV curves (E_{10}, η_{10}, j_{max}) are depicted in Table 6.

The ECs with best OER activity are Co/N-BioC and Co,Ni/N-BioC with j_{max} of 42.6 and 25.5 mA cm^{-2}, and an overpotential of 0.48 and 0.51 V, respectively. Ni/N-BioC and Fe/N-BioC have intermediate OER performance, with current densities of 13.9 and 10.1 mA cm^{-2}, respectively. These also show low overpotential of 0.55 and 0.63 V, respectively. The electrocatalysts with poorest OER activity are BioC, N/S-BioC, N-BioC, Pd/N-BioC, V/N-BioC, Cu/N-BioC and Zn/N-BioC, with current densities between 0.28 and 1.47 mA cm^{-2}.
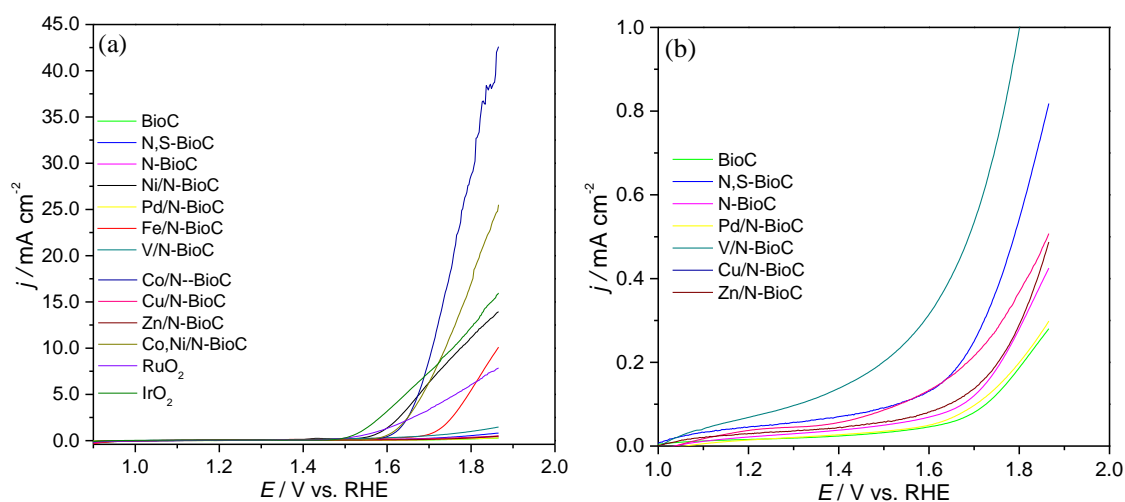
Figure 26 – (a) OER polarization curves for BioC, N/S-BioC, N-BioC, Ni/N-BioC, Pd/N-BioC, Fe/N-BioC, V/N-BioC, Co/N-BioC, Cu/N-BioC, Zn/N-BioC, Co,Ni/N-BioC, RuO_2 and IrO_2 and (b) OER polarization curves for BioC, N,S-BioC, N-BioC, Pd/N-BioC, V/N-BioC, Cu/N-BioC and Zn/N-BioC.

Table 6 – OER activity parameters (required potential to reach j = 10 mA cm^{-2}, overpotential, maximum current density and Tafel slope) for BioC, N/S-BioC, N-BioC, Ni/N-BioC, Pd/N-BioC, Fe/N-BioC, V/N-BioC, Co/N-BioC, Cu/N-BioC, Zn/N-BioC, Co,Ni/N-BioC and state-of-the-art OER electrocatalysts (RuO_2 and IrO_2).

Sample	E_{10} (V vs. RHE)	η_{10} (V)	j_{max} (mA cm^{-2})	TS (mV dec^{-1})
BioC	-	-	0.28	-
N/S-BioC	-	-	0.82	-
N-BioC	-	-	0.43	-
Ni/N-Bio	1.78	0.55	13.9	99
Pd/N-BioC	-		0.30	-
Fe/N-BioC	1.86	0.63	10.1	105
V/N-BioC	-	-	1.47	-
Co/N-BioC	1.71	0.48	42.6	74
Cu/N-BioC	-	-	0.51	-
Zn/N-BioC	-	-	0.49	-
Co,Ni/N-BioC	1.74	0.51	25.5	74
RuO$_2$	-	-	7.88	-
IrO$_2$	1.76	0.53	16.0	-

As for the ORR studies, the Tafel slopes were determined from the LSV curves and the Tafel plots are shown in Figure 27. The weak behaviour toward OER of certain materials did not allow the determination of their Tafel slopes and for this reason only the results of Ni/N-BioC, Fe/N-BioC, Co/N-BioC and Co,Ni/N-BioC are given. The lowest TS was obtained for Co/N-BioC and Co,Ni/N-BioC with 74 mV dec^{-1} followed by Ni/N-BioC (99 mV dec^{-1}) and Fe/N-BioC (113 mV dec^{-1}). These results support the previous claims that Co/N-BioC and Co,Ni/N-BioC are the most promising OER electrocatalysts (low Tafel slope, low overpotential and high current density).
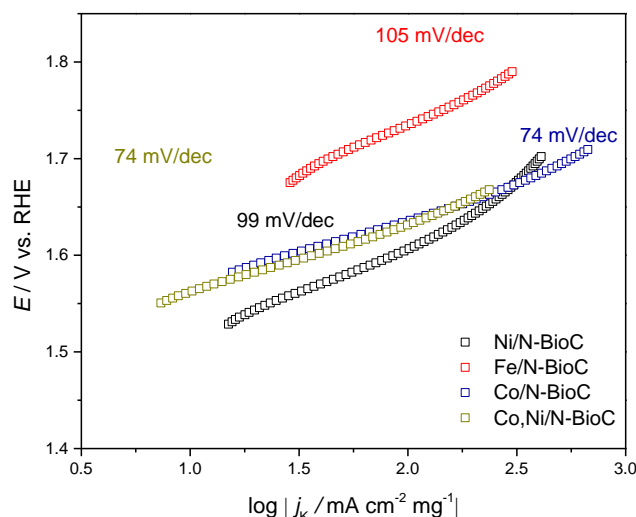
Figure 27 – OER Tafel slopes of Ni/N-BioC, Fe/N-BioC, Co/N-BioC and Co,Ni/N-BioC.

Stability tests were also performed to evaluate the OER performance over a long period of time (12 hours). The Chronoamperometric responses of Fe/N-BioC (a), Co/N-BioC (b) and Co,Ni/N-BioC (c) are displayed in Figure 28. As can be observed, the chronoamperometric plots show the characteristic local current density drops originated by oxygen bubble formation on the electrode surface, although previous current density values are in some cases partially recovered with bubble release.[80] From the three materials evaluated Co,Ni/N-BioC presented the best performance with a current retention of 75% after 12h. In contrast, Co/N-BioC lost close to 65% of its initial current. This may be attributed to the bubble release which can remove some amount of electrocatalysts from the electrode surface, leading to a decrease of OER current due to EC lost. For the Fe/N-BioC a strange behaviour was observed as initially there is an increase in the OER current over time followed

by the expected small decrease. This test was repeated and the same behaviour observed however, future studies must be conducted in order to understand it.
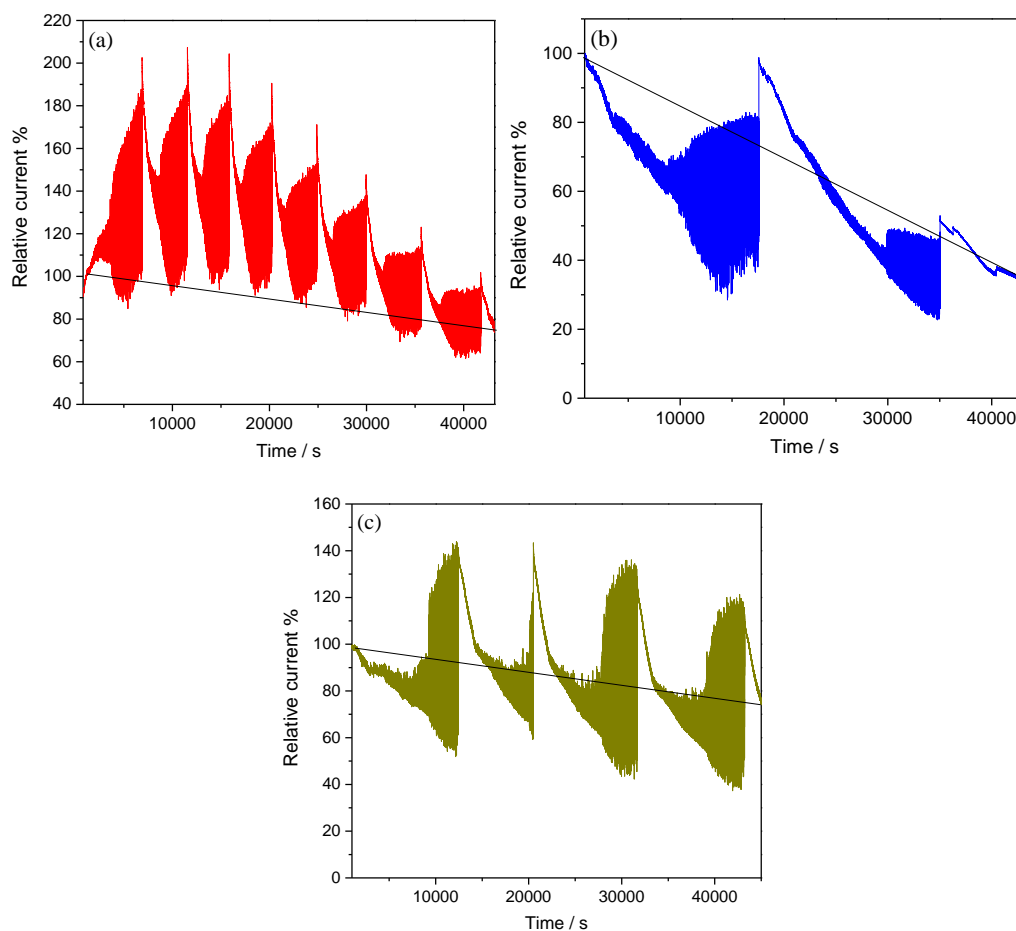
Figure 28 – Chronoamperometric plots of (a) Fe/N-BioC and (b) Co/N-BioC and (c) Co,Ni/N-BioC.

As for the ORR studies, Co/N-BioC was compared with similar previously reported materials. In Table 7, are presented the main results for different cobalt-containing N-doped carbon materials. The results obtained for Co/N-BioC are very similar but with the advantage that the carbon material used was prepared using biomass waste like vinery pruning wastes. As above, direct comparison is difficult because we still need to perform XPS analysis to determine the elements content as well as the type of N atoms present in the final carbon material after nitrogen doping and carbonization.

Table 7 – Comparison of OER activity parameters for different cobalt carbon materials doped with nitrogen.

Sample	E_{10} (V vs. RHE)	η_{10} (V)	TS (mV dec^{-1})	Ref.
Co/N-BioC	1.71	0.48	74	This work
Co@N-C	1.63	0.40	-	[104]
Co@N-CNFs	1.67	0.44	105	[105]
CF-NG-Co	1.63	0.40	60	[102]
CoO/N-doped carbon	1.57	0.34	71	[106]
N/Co-doped PCP//NRGO	1.66	0.43	292	[101]
Co-N-CNT frameworks	1.60	0.37	93	[103]

Chapter 4- Conclusions and future prospects

4. Conclusions and Future Prospects

Biomass-derived materials as electrocatalysts is still in an exploratory stage, however compared to other nitrogen-doped carbon materials, the biochars that were successfully prepared in this work, have the advantage of being eco-friendly, low-cost, and sustainable.

This work was divided into four stages: i) Preparation of biochar and heteroatom-doped biochar; ii) Preparation of novel composite materials based on doped biochar and metals; iii) materials characterization and iv) evaluation of their electrocatalytic abilities in ORR and OER.

First, to prove the activation of the hydrochar by CO_2 carbonization, CHNS analysis was made. The percentages of carbon, hydrogen, nitrogen, and oxygen confirm the successful activation. By ICP-OES, the incorporation of cobalt, copper, iron, nickel, palladium, vanadium, and zinc into the nitrogen-doped biochar was confirmed and the respective metals concentration determined. With SEM/EDS the morphology and the elements that were present in all materials were also confirmed. These characterization techniques allowed to confirm that all materials envisaged were successfully prepared.

In electrocatalysis, the Co/N-BioC was the material that showed the best performance for ORR and OER. The Co/N-BioC showed a n_{O_2} value close to 4, which indicates a 4-electron mechanism, a good tolerance to methanol (93%) and good ORR activity with an E_{onset} and j_L values of 0.86 V vs. RHE and -3.48 mA cm^{-2}, respectively. Furthermore, Co/N-BioC also showed a good OER activity, with η_{10} and j_{max} values of 0.48 V and 42.6 mA cm^{-2}.

As future work, some improvements can be made to further optimize the electrocatalysts performance to achieve the standard ORR electrocatalytic performance of the state-of-the-art Pt/C catalyst. In the synthesis of biochars, the nitrogen source was phenanthroline which can be changed to melamine, and XPS analysis needs to be done to understand the type of nitrogen since the ORR activity of N-doped carbon strongly depends on the nitrogen configuration.

In Co,Ni-BioC it was expected a better ORR and OER performance so, further studies are needed to understand what might be blocking the performance of this electrocatalyst. Additionally, the preparation of biochars with a mixture of different metals such as Co,Fe/N-BioC and Fe/Ni-BioC may be a good alternative, as some studies show that the efficiency of carbon materials with these mixtures of metals are promising.

Chapter 5- References

5. References

1.   Katsounaros, I.; Cherevko, S.; Zeradjanin, A. R.; Mayrhofer, K. J. J., Oxygen Electrochemistry as a Cornerstone for Sustainable Energy Conversion. *Angewandte Chemie-International Edition* **2014,** *53* (1), 102-121.

2.   Ambrosi, A.; Chua, C. K.; Bonanni, A.; Pumera, M., Electrochemistry of Graphene and Related Materials. *Chemical Reviews* **2014,** *114* (14), 7150-7188.

3.   Fernandes, D. M.; Mathumba, P.; Fernandes, A. J. S.; Iwuoha, E. I.; Freire, C., Towards efficient oxygen reduction reaction electrocatalysts through graphene doping. *Electrochimica Acta* **2019,** *319*, 72-81.

4.   Kim, B. K.; Sy, S.; Yu, A.; Zhang, J., Electrochemical Supercapacitors for Energy Storage and Conversion. In *Handbook of Clean Energy Systems*, 2015; pp 1-25.

5.   Gao, S.; Li, X.; Li, L.; Wei, X., A versatile biomass derived carbon material for oxygen reduction reaction, supercapacitors and oil/water separation. *Nano Energy* **2017,** *33*, 334-342.

6.   Freire, C.; Fernandes, D. M.; Nunes, M.; Abdelkader, V. K., POM & MOF-based Electrocatalysts for Energy-related Reactions. *ChemCatChem* **2018,** *10* (8), 1703-1730.

7.   Seh, Z. W.; Kibsgaard, J.; Dickens, C. F.; Chorkendorff, I.; Norskov, J. K.; Jaramillo, T. F., Combining theory and experiment in electrocatalysis: Insights into materials design. *Science* **2017,** *355* (6321).

8.   Winter, M.; Brodd, R. J., What are batteries, fuel cells, and supercapacitors? *Chemical Reviews* **2004,** *104* (10), 4245-4269.

9.   Abdelkareem, M. A.; Elsaid, K.; Wilberforce, T.; Kamil, M.; Sayed, E. T.; Olabi, A., Environmental aspects of fuel cells: A review. *Sci Total Environ* **2021,** *752*, 141803.

10.   Zhang, F.; Miao, J.; Liu, W.; Xu, D.; Li, X., Heteroatom embedded graphene-like structure anchored on porous biochar as efficient metal-free catalyst for ORR. *International Journal of Hydrogen Energy* **2019,** *44* (59), 30986-30998.

11.   Society, A. C., *ISE Chemistry in Context*. McGraw-Hill Education: 2020.

12.   Shao, M.; Chang, Q.; Dodelet, J. P.; Chenitz, R., Recent Advances in Electrocatalysts for Oxygen Reduction Reaction. *Chem Rev* **2016,** *116* (6), 3594-657.

13.   Fernandes, D. M.; Novais, H. C.; Bacsa, R.; Serp, P.; Bachiller-Baeza, B.; Rodriguez-Ramos, I.;   Guerrero-Ruiz, A.; Freire, C., Polyoxotungstate@Carbon Nanocomposites As Oxygen Reduction Reaction (ORR) Electrocatalysts. *Langmuir* **2018,** *34* (22), 6376-6387.

14.   Shi, H.; Shen, Y.; He, F.; Li, Y.; Liu, A.; Liu, S.; Zhang, Y., Recent advances of doped carbon as non-precious catalysts for oxygen reduction reaction. *J. Mater. Chem. A* **2014,** *2* (38), 15704-15716.

15.   Zhang, M.; Dai, L., Carbon nanomaterials as metal-free catalysts in next generation fuel cells. *Nano Energy* **2012,** *1* (4), 514-517.

16.   Jiao, Y.; Zheng, Y.; Jaroniec, M. T.; Qiao, S. Z., Design of electrocatalysts for oxygen- and hydrogen-involving energy conversion reactions. *Chemical Society Reviews* **2015,** *44* (8), 2060-2086.

17.   Chu, S.; Cui, Y.; Liu, N., The path towards sustainable energy. *Nat Mater* **2016,** *16* (1), 16-22.

18.   Feng, C.; Faheem, M. B.; Fu, J.; Xiao, Y.; Li, C.; Li, Y., Fe-Based Electrocatalysts for Oxygen Evolution Reaction: Progress and Perspectives. *ACS Catalysis* **2020,** *10* (7), 4019-4047.

19.   Kaur, M.; Pal, K., Review on hydrogen storage materials and methods from an electrochemical viewpoint. *Journal of Energy Storage* **2019,** *23*, 234-249.

20.   Hong, W. T.; Risch, M.; Stoerzinger, K. A.; Grimaud, A.; Suntivich, J.; Shao-Horn, Y., Toward the rational design of non-precious transition metal oxides for oxygen electrocatalysis. *Energy & Environmental Science* **2015,** *8* (5), 1404-1427.

21.   Kuang, M.; Zheng, G., Nanostructured Bifunctional Redox Electrocatalysts. *Small* **2016,** *12* (41), 5656-5675.

22.   Li, S.; Thomas, A., Emerged carbon nanomaterials from metal-organic precursors for electrochemical catalysis in energy conversion. In *Advanced Nanomaterials for Electrochemical-Based Energy Conversion and Storage*, 2020; pp 393-423.

23.   Guy, O. J.; Walker, K.-A. D., Graphene Functionalization for Biosensor Applications. In *Silicon Carbide Biotechnology*, 2016; pp 85-141.

24.   Bontempelli, G.; Dossi, N.; Toniolo, R., Linear Sweep and Cyclic☆. In *Reference Module in Chemistry, Molecular Sciences and Chemical Engineering*, 2016.

25.   Huang, Z.-F.; Wang, J.; Peng, Y.; Jung, C.-Y.; Fisher, A.; Wang, X., Design of Efficient Bifunctional Oxygen Reduction/Evolution Electrocatalyst: Recent Advances and Perspectives. *Advanced Energy Materials* **2017,** *7* (23).

26.   Zhou, R.; Jaroniec, M.; Qiao, S.-Z., Nitrogen-Doped Carbon Electrocatalysts Decorated with Transition Metals for the Oxygen Reduction Reaction. *ChemCatChem* **2015,** *7* (23), 3808-3817.

27.   Abdelkader-Fernández, V. K.; Fernandes, D. M.; Balula, S. S.; Cunha-Silva, L.; Freire, C., Oxygen Evolution Reaction Electrocatalytic Improvement in POM@ZIF Nanocomposites: A Bidirectional Synergistic Effect. *ACS Applied Energy Materials* **2020,** *3* (3), 2925-2934.

28.   Anantharaj, S.; Ede, S. R.; Sakthikumar, K.; Karthick, K.; Mishra, S.; Kundu, S., Recent Trends and Perspectives in Electrochemical Water Splitting with an Emphasis on

Sulfide, Selenide, and Phosphide Catalysts of Fe, Co, and Ni: A Review. *ACS Catalysis* **2016,** *6* (12), 8069-8097.

29.   Liu, W.-J.; Jiang, H.; Yu, H.-Q., Emerging applications of biochar-based materials for energy storage and conversion. *Energy & Environmental Science* **2019,** *12* (6), 1751-1779.

30.   Zhang, C.; Shen, X.; Pan, Y.; Peng, Z., A review of Pt-based electrocatalysts for oxygen reduction reaction. *Frontiers in Energy* **2017,** *11* (3), 268-285.

31.   Dun, R.; Hao, M.; Su, Y.; Li, W., Fe–N-doped hierarchical mesoporous carbon nanomaterials as efficient catalysts for oxygen reduction in both acidic and alkaline media. *Journal of Materials Chemistry A* **2019,** *7* (20), 12518-12525.

32.   Gao, K.; Wang, B.; Tao, L.; Cunning, B. V.; Zhang, Z.; Wang, S.; Ruoff, R. S.; Qu, L., Efficient Metal-Free Electrocatalysts from N-Doped Carbon Nanomaterials: Mono-Doping and Co-Doping. *Adv Mater* **2019,** *31* (13), e1805121.

33.   Gao, S.; Li, L.; Geng, K.; Wei, X.; Zhang, S., Recycling the biowaste to produce nitrogen and sulfur self-doped porous carbon as an efficient catalyst for oxygen reduction reaction. *Nano Energy* **2015,** *16*, 408-418.

34.   Zhu, Y. L.; Zhou, W.; Yu, J.; Chen, Y. B.; Liu, M. L.; Shao, Z. P., Enhancing Electrocatalytic Activity of Perovskite Oxides by Tuning Cation Deficiency for Oxygen Reduction and Evolution Reactions. *Chemistry of Materials* **2016,** *28* (6), 1691-1697.

35.   Frackowiak, E.; Beguin, F., Carbon materials for the electrochemical storage of energy in capacitors. *Carbon* **2001,** *39* (6), 937-950.

36.   Wang, Y. G.; Song, Y. F.; Xia, Y. Y., Electrochemical capacitors: mechanism, materials, systems, characterization and applications. *Chemical Society Reviews* **2016,** *45* (21), 5925-5950.

37.   Cheng, B. H.; Zeng, R. J.; Jiang, H., Recent developments of post-modification of biochar for electrochemical energy storage. *Bioresour Technol* **2017,** *246*, 224-233.

38.   Qin, C.; Wang, H.; Yuan, X.; Xiong, T.; Zhang, J.; Zhang, J., Understanding structure-performance correlation of biochar materials in environmental remediation and electrochemical devices. *Chemical Engineering Journal* **2020,** *382*.

39.   Zhu, Y. P.; Guo, C.; Zheng, Y.; Qiao, S. Z., Surface and Interface Engineering of Noble-Metal-Free Electrocatalysts for Efficient Energy Conversion Processes. *Acc Chem Res* **2017,** *50* (4), 915-923.

40.   Ma, R.; Lin, G.; Zhou, Y.; Liu, Q.; Zhang, T.; Shan, G.; Yang, M.; Wang, J., A review of oxygen reduction mechanisms for metal-free carbon-based electrocatalysts. *npj Computational Materials* **2019,** *5* (1).

41.   Fernandes, D. M.; Peixoto, A. F.; Freire, C., Nitrogen-doped metal-free carbon catalysts for (electro)chemical CO2 conversion and valorisation. *Dalton Trans* **2019,** *48* (36), 13508-13528.

42.   Jarrais, B.; Guedes, A.; Freire, C., Heteroatom-Doped Carbon Nanomaterials as Metal-Free Catalysts for the Reduction of 4-Nitrophenol. *ChemistrySelect* **2018,** *3* (6), 1737-1748.

43.   Trogadas, P.; Fuller, T. F.; Strasser, P., Carbon as catalyst and support for electrochemical energy conversion. *Carbon* **2014,** *75*, 5-42.

44.   Osmieri, L.; Escudero-Cid, R.; Armandi, M.; Monteverde Videla, A. H. A.; García Fierro, J. L.; Ocón, P.; Specchia, S., Fe-N/C catalysts for oxygen reduction reaction supported on different carbonaceous materials. Performance in acidic and alkaline direct alcohol fuel cells. *Applied Catalysis B: Environmental* **2017,** *205*, 637-653.

45.   Wang, J.; Cui, W.; Liu, Q.; Xing, Z.; Asiri, A. M.; Sun, X., Recent Progress in Cobalt-Based Heterogeneous Catalysts for Electrochemical Water Splitting. *Adv Mater* **2016,** *28* (2), 215-30.

46.   Chen, T.; Guo, S.; Yang, J.; Xu, Y.; Sun, J.; Wei, D.; Chen, Z.; Zhao, B.; Ding, W., Nitrogen-Doped Carbon Activated in Situ by Embedded Nickel through the Mott-Schottky Effect for the Oxygen Reduction Reaction. *Chemphyschem* **2017,** *18* (23), 3454-3461.

47.   Li, Y.; Li, Q.; Wang, H.; Zhang, L.; Wilkinson, D. P.; Zhang, J., Recent Progresses in Oxygen Reduction Reaction Electrocatalysts for Electrochemical Energy Applications. *Electrochemical Energy Reviews* **2019,** *2* (4), 518-538.

48.   Zhang, J.; Xia, Z.; Dai, L., Carbon-based electrocatalysts for advanced energy conversion and storage. *Science advances* **2015,** *1* (7), e1500564.

49.   Lefevre, M.; Proietti, E.; Jaouen, F.; Dodelet, J. P., Iron-based catalysts with improved oxygen reduction activity in polymer electrolyte fuel cells. *Science* **2009,** *324* (5923), 71-4.

50.   Guo, C.; Liao, W.; Li, Z.; Chen, C., Exploration of the catalytically active site structures of animal biomass-modified on cheap carbon nanospheres for oxygen reduction reaction with high activity, stability and methanol-tolerant performance in alkaline medium. *Carbon* **2015,** *85*, 279-288.

51.   Cao, X.; Sun, S.; Sun, R., Application of biochar-based catalysts in biomass upgrading: a review. *RSC Adv.* **2017,** *7* (77), 48793-48805.

52.   Lee, J.; Kim, K.-H.; Kwon, E. E., Biochar as a Catalyst. *Renewable and Sustainable Energy Reviews* **2017,** *77*, 70-79.

53.   Wang, J.-R.; Wan, F.; Lü, Q.-F.; Chen, F.; Lin, Q., Self-nitrogen-doped porous biochar derived from kapok (Ceiba insignis) fibers: Effect of pyrolysis temperature and high electrochemical performance. *Journal of Materials Science & Technology* **2018,** *34* (10), 1959-1968.

54.   Rahman, M. Z.; Edvinsson, T.; Kwong, P., Biochar for electrochemical applications. *Current Opinion in Green and Sustainable Chemistry* **2020,** *23*, 25-30.

55. Senthil, C.; Lee, C. W., Biomass-derived biochar materials as sustainable energy sources for electrochemical energy storage devices. *Renewable and Sustainable Energy Reviews* **2021,** *137*.

56. Liu, W. J.; Jiang, H.; Yu, H. Q., Development of Biochar-Based Functional Materials: Toward a Sustainable Platform Carbon Material. *Chem Rev* **2015,** *115* (22), 12251-85.

57. Dai, Y.; Zhang, N.; Xing, C.; Cui, Q.; Sun, Q., The adsorption, regeneration and engineering applications of biochar for removal organic pollutants: A review. *Chemosphere* **2019,** *223*, 12-27.

58. Chen, W.; Yang, H.; Chen, Y.; Chen, X.; Fang, Y.; Chen, H., Biomass pyrolysis for nitrogen-containing liquid chemicals and nitrogen-doped carbon materials. *Journal of Analytical and Applied Pyrolysis* **2016,** *120*, 186-193.

59. Nieva Lobos, M. L.; Sieben, J. M.; Comignani, V.; Duarte, M.; Volpe, M. A.; Moyano, E. L., Biochar from pyrolysis of cellulose: An alternative catalyst support for the electro-oxidation of methanol. *International Journal of Hydrogen Energy* **2016,** *41* (25), 10695-10706.

60. Zhang, M.; Jin, X.; Wang, L.; Sun, M.; Tang, Y.; Chen, Y.; Sun, Y.; Yang, X.; Wan, P., Improving biomass-derived carbon by activation with nitrogen and cobalt for supercapacitors and oxygen reduction reaction. *Applied Surface Science* **2017,** *411*, 251-260.

61. Wang, K.; Wang, H.; Ji, S.; Feng, H.; Linkov, V.; Wang, R., Biomass-derived activated carbon as high-performance non-precious electrocatalyst for oxygen reduction. *RSC Advances* **2013,** *3* (30).

62. Chacón, F. J.; Cayuela, M. L.; Roig, A.; Sánchez-Monedero, M. A., Understanding, measuring and tuning the electrochemical properties of biochar for environmental applications. *Reviews in Environmental Science and Bio/Technology* **2017,** *16* (4), 695-715.

63. Huang, W. H.; Lee, D. J.; Huang, C., Modification on biochars for applications: A research update. *Bioresour Technol* **2021,** *319*, 124100.

64. Shan, R.; Han, J.; Gu, J.; Yuan, H.; Luo, B.; Chen, Y., A review of recent developments in catalytic applications of biochar-based materials. *Resources, Conservation and Recycling* **2020,** *162*.

65. Li, M.; Xiong, Y.; Liu, X.; Han, C.; Zhang, Y.; Bo, X.; Guo, L., Iron and nitrogen co-doped carbon nanotube@hollow carbon fibers derived from plant biomass as efficient catalysts for the oxygen reduction reaction. *Journal of Materials Chemistry A* **2015,** *3* (18), 9658-9667.

66. Borghei, M.; Laocharoen, N.; Kibena-Põldsepp, E.; Johansson, L.-S.; Campbell, J.; Kauppinen, E.; Tammeveski, K.; Rojas, O. J., Porous N,P-doped carbon from coconut shells with high electrocatalytic activity for oxygen reduction: Alternative to Pt-C for alkaline fuel cells. *Applied Catalysis B: Environmental* **2017,** *204*, 394-402.

67.   Yuan, W.; Feng, Y.; Xie, A.; Zhang, X.; Huang, F.; Li, S.; Zhang, X.; Shen, Y., Nitrogen-doped nanoporous carbon derived from waste pomelo peel as a metal-free electrocatalyst for the oxygen reduction reaction. *Nanoscale* **2016,** *8* (16), 8704-11.

68.   Gao, S.; Wei, X.; Fan, H.; Li, L.; Geng, K.; Wang, J., Nitrogen-doped carbon shell structure derived from natural leaves as a potential catalyst for oxygen reduction reaction. *Nano Energy* **2015,** *13*, 518-526.

69.   Xiong, X.; Jiang, R.; Deng, B.; Yang, J.; Wang, D., Bionic Structural Design and Electrochemical Manufacture of WC/N-Doped Carbon Hybrids as Efficient ORR Catalyst. *Journal of The Electrochemical Society* **2020,** *167* (6).

70.   Liu, X.; Zhou, Y.; Zhou, W.; Li, L.; Huang, S.; Chen, S., Biomass-derived nitrogen self-doped porous carbon as effective metal-free catalysts for oxygen reduction reaction. *Nanoscale* **2015,** *7* (14), 6136-42.

71.   Ma, L.-L.; Liu, W.-J.; Hu, X.; Lam, P. K. S.; Zeng, J. R.; Yu, H.-Q., Ionothermal carbonization of biomass to construct sp2/sp3 carbon interface in N-doped biochar as efficient oxygen reduction electrocatalysts. *Chemical Engineering Journal* **2020,** *400*.

72.   Peixoto, A. F.; Ramos, R.; Moreira, M. M.; Soares, O. S. G. P.; Ribeiro, L. S.; Pereira, M. F. R.; Delerue-Matos, C.; Freire, C., Production of ethyl levulinate fuel bioadditive from 5-hydroxymethylfurfural over sulfonic acid functionalized biochar catalysts. *Fuel* **2021,** *303*.

73.   Jagadeesh, R. V.; Stemmler, T.; Surkus, A. E.; Junge, H.; Junge, K.; Beller, M., Hydrogenation using iron oxide-based nanocatalysts for the synthesis of amines. *Nature Protocols* **2015,** *10* (4), 548-557.

74.   Evaluation of analytical instrumentation. Part XIX CHNS elemental analysers. *Accreditation and Quality Assurance* **2006,** *11* (11), 569-576.

75.   Thompson, M., CHNS elemental analysers. *AMC Technical Briefs. RSC* **2008**.

76.   Levine, M. ICP-OES – ICP Chemistry, ICP-OES Analysis, Strengths and Limitations. https://www.technologynetworks.com/analysis/articles/icp-oes-icp-chemistry-icp-oes-analysis-strengths-and-limitations-342265 (accessed May 17, 2021).

77.   Skoog, D. A.; Leary, J. J., *Principles of Instrumental Analysis*. 4th ed.; 1992.

78.   Ferreira, P.; Abreu, B.; Freire, C.; Fernandes, D. M.; Marques, E. F., Nanocomposites Prepared from Carbon Nanotubes and the Transition Metal Dichalcogenides WS2 and MoS2 via Surfactant-Assisted Dispersions as Electrocatalysts for Oxygen Reactions. *Materials* **2021,** *14* (4).

79.   Abdelkader-Fernández, V. K.; Fernandes, D. M.; Balula, S. S.; Cunha-Silva, L.; Pérez-Mendoza, M. J.; López-Garzón, F. J.; Pereira, M. F.; Freire, C., Noble-Metal-Free MOF-74-Derived Nanocarbons: Insights on Metal Composition and Doping Effects on the Electrocatalytic Activity Toward Oxygen Reactions. *ACS Applied Energy Materials* **2019,** *2* (3), 1854-1867.

80.   Abdelkader-Fernández, V. K.; Fernandes, D. M.; Balula, S. S.; Cunha-Silva, L.; Freire, C., Advanced framework-modified POM@ZIF-67 nanocomposites as enhanced oxygen evolution reaction electrocatalysts. *Journal of Materials Chemistry A* **2020,** *8* (27), 13509-13521.

81.   Ahmad, A. A.; Idris, A., Preparation and characterization of activated carbons derived from bio-solid: a review. *Desalination and Water Treatment* **2013,** *52* (25-27), 4848-4862.

82.   Tsamba, A. J.; Yang, W.; Blasiak, W., Pyrolysis characteristics and global kinetics of coconut and cashew nut shells. *Fuel Processing Technology* **2006,** *87* (6), 523-530.

83.   Ozdemir, I.; Şahin, M.; Orhan, R.; Erdem, M., Preparation and characterization of activated carbon from grape stalk by zinc chloride activation. *Fuel Processing Technology* **2014,** *125*, 200-206.

84.   Tientong, J.; Garcia, S.; Thurber, C. R.; Golden, T. D., Synthesis of Nickel and Nickel Hydroxide Nanopowders by Simplified Chemical Reduction. *Journal of Nanotechnology* **2014,** *2014*, 1-6.

85.   Kim, D.-S.; Kim, T.-J.; Kim, J.-H.; Zeid, E. F. A.; Kim, Y.-T., Fine Structure Effect of PdCo electrocatalyst for Oxygen Reduction Reaction Activity: Based on X-ray Absorption Spectroscopy Studies with Synchrotron Beam. *Journal of Electrochemical Science and Technology* **2010,** *1* (1), 31-38.

86.   Santos, J. L.; Mäki-Arvela, P.; Monzón, A.; Murzin, D. Y.; Centeno, M. Á., Metal catalysts supported on biochars: Part I synthesis and characterization. *Applied Catalysis B: Environmental* **2020,** *268*.

87.   Zhou, Y.; Wang, C.; Peng, X.; Zhang, T.; Wang, X.; Jiang, Y.; Qi, H.; Zheng, L.; Lin, J.; Jiang, L., Boosting Efficient Ammonia Synthesis over Atomically Dispersed Co-Based Catalyst via the Modulation of Geometric and Electronic Structures. *CCS Chemistry* **2021**, 1881-1892.

88.   Pei, Z.; Huang, Y.; Tang, Z.; Ma, L.; Liu, Z.; Xue, Q.; Wang, Z.; Li, H.; Chen, Y.; Zhi, C., Enabling highly efficient, flexible and rechargeable quasi-solid-state zn-air batteries via catalyst engineering and electrolyte functionalization. *Energy Storage Materials* **2019,** *20*, 234-242.

89.   Batool, M., Degradation of Malachite Green by Green Synthesized Copper Nanoparticles by Using Aloe Barbadensis Leaf Extracts. *Archives of Nanomedicine: Open Access Journal* **2018,** *1* (2).

90.   Cheng, H.-H.; Chen, S.-S.; Liu, H.-M.; Jang, L.-W.; Chang, S.-Y., Glycine–Nitrate Combustion Synthesis of Cu-Based Nanoparticles for NP9EO Degradation Applications. *Catalysts* **2020,** *10* (9).

91.   Zhang, B.; Chen, J.; Guo, H.; Le, M.; Guo, H.; Li, Z.; Wang, L., Iron Carbide Nanoparticles Supported by Nitrogen-Doped Carbon Nanosheets for Oxygen Reduction. *ACS Applied Nano Materials* **2021,** *4* (8), 8360-8367.

92.   Hou, Z. Q.; Wang, Z. Y.; Yang, L. X.; Yang, Z. G., Nitrogen-doped reduced graphene oxide intertwined with V2O3 nanoflakes as self-supported electrodes for flexible all-solid-state supercapacitors. *RSC Advances* **2017,** *7* (41), 25732-25739.

93.   Fernandes, D. M.; Abdelkader-Fernández, V. K.; Badenhorst, C.; Bialecka, B.; Guedes, A.; Predeanu, G.; Santos, A. C.; Valentim, B.; Wagner, N.; Freire, C., Coal chars recovered from fly ash as promising electrocatalysts for oxygen reduction reaction. *International Journal of Hydrogen Energy* **2021**.

94.   Fernandes, D. M.; Mestre, A. S.; Martins, A.; Nunes, N.; Carvalho, A. P.; Freire, C., Biomass-derived nanoporous carbons as electrocatalysts for oxygen reduction reaction. *Catalysis Today* **2020,** *357*, 269-278.

95.   Su, Y. H.; Zhu, Y. H.; Jiang, H. L.; Shen, J. H.; Yang, X. L.; Zou, W. J.; Chen, J. D.; Li, C. Z., Cobalt nanoparticles embedded in N-doped carbon as an efficient bifunctional electrocatalyst for oxygen reduction and evolution reactions. *Nanoscale* **2014,** *6* (24), 15080-15089.

96.   Shinagawa, T.; Garcia-Esparza, A. T.; Takanabe, K., Insight on Tafel slopes from a microkinetic analysis of aqueous electrocatalysis for energy conversion. *Sci Rep* **2015,** *5*, 13801.

97.   Jiang, Y. Y.; Ni, P. J.; Chen, C. X.; Lu, Y. Z.; Yang, P.; Kong, B.; Fisher, A.; Wang, X., Selective Electrochemical H2O2 Production through Two-Electron Oxygen Electrochemistry. *Advanced Energy Materials* **2018,** *8* (31).

98.   Ye, Y. Y.; Qian, T. T.; Jiang, H., Co-Loaded N-Doped Biochar as a High-Performance Oxygen Reduction Reaction Electrocatalyst by Combined Pyrolysis of Biomass. *Industrial & Engineering Chemistry Research* **2020,** *59* (35), 15614-15623.

99.   Yin, P. Q.; Yao, T.; Wu, Y.; Zheng, L. R.; Lin, Y.; Liu, W.; Ju, H. X.; Zhu, J. F.; Hong, X.; Deng, Z. X.; Zhou, G.; Wei, S. Q.; Li, Y. D., Single Cobalt Atoms with Precise N-Coordination as Superior Oxygen Reduction Reaction Catalysts. *Angewandte Chemie-International Edition* **2016,** *55* (36), 10800-10805.

100.   Liu, Y.; Jiang, H.; Zhu, Y.; Yang, X.; Li, C., Transition metals (Fe, Co, and Ni) encapsulated in nitrogen-doped carbon nanotubes as bi-functional catalysts for oxygen electrode reactions. *Journal of Materials Chemistry A* **2016,** *4* (5), 1694-1701.

101.   Hou, Y.; Wen, Z.; Cui, S.; Ci, S.; Mao, S.; Chen, J., An Advanced Nitrogen-Doped Graphene/Cobalt-Embedded Porous Carbon Polyhedron Hybrid for Efficient Catalysis of Oxygen Reduction and Water Splitting. *Advanced Functional Materials* **2015,** *25* (6), 872-882.

102.   Pei, Z.; Tang, Z.; Liu, Z.; Huang, Y.; Wang, Y.; Li, H.; Xue, Q.; Zhu, M.; Tang, D.; Zhi, C., Construction of a hierarchical 3D Co/N-carbon electrocatalyst for efficient oxygen reduction and overall water splitting. *Journal of Materials Chemistry A* **2018,** *6* (2), 489-497.

103.   Xia, B. Y.; Yan, Y.; Li, N.; Wu, H. B.; Lou, X. W.; Wang, X., A metal–organic framework-derived bifunctional oxygen electrocatalyst. *Nature Energy* **2016,** *1* (1).

104.   Wang, J.; Gao, D.; Wang, G.; Miao, S.; Wu, H.; Li, J.; Bao, X., Cobalt nanoparticles encapsulated in nitrogen-doped carbon as a bifunctional catalyst for water electrolysis. *J. Mater. Chem. A* **2014,** *2* (47), 20067-20074.

105.   Li, T.; Li, S.; Liu, Q.; Yin, J.; Sun, D.; Zhang, M.; Xu, L.; Tang, Y.; Zhang, Y., Immobilization of Ni3Co Nanoparticles into N-Doped Carbon Nanotube/Nanofiber Integrated Hierarchically Branched Architectures toward Efficient Overall Water Splitting. *Adv Sci (Weinh)* **2020,** *7* (1), 1902371.

106.   Mao, S.; Wen, Z.; Huang, T.; Hou, Y.; Chen, J., High-performance bi-functional electrocatalysts of 3D crumpled graphene–cobalt oxide nanohybrids for oxygen reduction and evolution reactions. *Energy Environ. Sci.* **2014,** *7* (2), 609-616.